High-temperature alteration during cooling of mafic intrusions: Insights from the Saint-Jean-du-Doigt intrusive complex (Armorican Massif, France)

Anthony Pochon, Giada Iacono-Marziano, Eric Gloaguen, Johann Tuduri, Saskia Erdmann

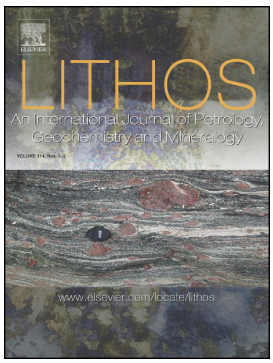

High-temperature alteration during cooling of mafic intrusions: Insights from the Saint-Jean-du-Doigt intrusive complex (Armorican Massif, France)

Anthony Pochon, Giada Iacono-Marziano, Eric Gloaguen, Johann Tuduri, Saskia Erdmann

PII: S0024-4937(22)00386-3

DOI: https://doi.org/10.1016/j.lithos.2022.106977

Reference: LITHOS 106977

To appear in: *LITHOS*

Received date: 16 June 2022

Revised date: 4 November 2022

Accepted date: 25 November 2022

Please cite this article as: A. Pochon, G. Iacono-Marziano, E. Gloaguen, et al., High-temperature alteration during cooling of mafic intrusions: Insights from the Saint-Jean-du-Doigt intrusive complex (Armorican Massif, France), *LITHOS* (2022), https://doi.org/10.1016/j.lithos.2022.106977

High-temperature alteration during cooling of mafic intrusions: insights from the Saint-Jean-du-Doigt intrusive complex (Armorican Massif, France)

Anthony Pochon[1, 2]*, Giada Iacono-Marziano[1], Eric Gloaguen[1, 2], Johann Tuduri[1, 2], Saskia Erdmann[1]

[1] ISTO, UMR 7327, Université d'Orléans, CNRS, BRGM, F-45071 Orléans, France

[2] BRGM, F-45060 Orléans, France

* To whom correspondence may be addressed. Email: a.pochon@brgm.fr

Abstract

We characterize the alteration of the Saint-Jean-du-Doigt mafic-dominated, bimodal intrusive complex in the Armorican Massif by means of petrographic investigation and geochemical analysis. The pluton crops out along the seashore, providing a well-exposed, continuous E-W cross-section. The 3D geological modeling confirms that the western part corresponds to the lower part of the intrusion, whereas the eastern part represents the intrusion roof. The petrographic observations highlight an alteration gradient from the lower part to the intrusion roof. Whereas calcic plagioclase is well preserved in the lower part, it is partially saussuritized in the central part and completely altered to albite, epidote and sericite in the intrusion roof. Clinopyroxene is common and partially replaced by actinolite in the lower part, and absent in the intrusion roof. Amphibole is extremely common throughout the pluton. Mineralogical and chemical analyses of amphibole show a crystallization sequence from primary magmatic (brown) magnesio-hastingsite over transitional magnesio-hornblende to secondary actinolite, with a range of estimated crystallization temperatures between ~900 and ~450°C. Ilmenite crystals are fluid inclusion-rich in the central part and the intrusion roof, but fluid inclusion-free in the lower part. Qualitative analyses of the fluid inclusion-bearing ilmenite show that it is enriched in Mo, Sn, Sb, Pb and W, strongly suggesting that these elements are concentrated in the fluid phase. Fluid-inclusion bearing ilmenite of the upper part of the intrusion is then partially replaced by titanite and rutile at temperatures around 600°C. The abundance of hydrous mineral phases and pegmatites, common evidence for fluid-assisted mineral replacement, and volatiles trapped in ilmenite strongly suggest that the Saint-Jean-du-Doigt intrusive complex had a high volatile content. We therefore propose that the observed progressive alteration from the lower to the upper part of the intrusion mainly results from the interaction of the gabbroic rocks with exsolved magmatic fluids of the intrusive complex. We finally suggest that the petrological and geochemical features observed in the mafic rocks of the Saint-Jean-du-Doigt intrusive complex track the magmatic-hydrothermal transition of the pluton.

Keywords

Magmatic-hydrothermal processes, Ilmenite, Amphibole, Fluid inclusions, Autometasomatism

1. Introduction

Volatiles play a major role in the evolution of magmas from their generation in the mantle to ponding within the crust, and eventually eruption at the surface. Water, in particular, has a major effect on magma solidus and liquidus temperatures, rheological properties (Gonnermann and Manga, 2007), and magmatic differentiation paths (Grove et al., 2003; Zimmer et al., 2010). The abundance of H_2O then leads to particular late-magmatic mineral assemblages and strongly affects replacement processes, playing a catalytic and thermodynamic role (Putnis and Austrheim, 2010). Inherently, water is a key control for potential ore forming processes (Hedenquist and Lowenstern, 1994). The role and the importance of magmatic aqueous fluids in replacement and ore-forming processes is well established in intermediate-felsic systems, especially through numerous studies on porphyry deposits (Hedenquist and Lowenstern, 1994; Williams-Jones and Heinrich, 2005; Vigneresse et al., 2019). However, the role of magmatic aqueous fluids in ore forming processes related to upper crustal mafic magmas remains markedly less well-constrained than for felsic systems. With the exception of olivine alteration to iddingsite, which is typically considered to take place at magmatic conditions, alteration by magmatic fluids is rarely considered for mafic rocks.

A key reason for this is that distinguishing between metamorphic-derived mineral assemblages and late-stage magmatic or hydrothermal alteration assemblages is a challenging task because of their similarities (Mullan and Bussell, 1977). Indeed, the cooling and uplift of mafic plutons typically results in metamorphic reactions during decreasing pressure and temperature, resulting in the formation of albite + epidote + actinolite. Such mineral assemblage could also be the result of (i) high temperature alteration by magmatic fluids (sometimes called autometamorphism or autometasomatism, Mullan and Bussell, 1977; Elsdon, 1982 ; Pe-Piper et al., 2010), or (ii) hydrothermal alteration by meteoric or seawater fluids (Pertsev et al., 2015; Nicollet et al., 2022). To distinguish between these three types of alteration is thus important for mafic plutonic rocks in order to retrace their evolution from emplacement to cooling, including magmatic degassing.

For this purpose, we characterize the alteration of the early Carboniferous Saint-Jean-du-Doigt (SJDD) mafic-silicic pluton in the Armorican Massif (France). Petrogenetic and geochronological studies (Barboni et al., 2011, 2013; Caroff et al., 2011) have already been performed on this intrusive complex, making it an ideal target to study the magmatic-hydrothermal transition. In addition, the plutonic complex crops out along the seashore, providing a well-exposed continuous cross-section. We combine 3D geological modelling, field and microscopic observations, major- and trace-element analysis of minerals, and geothermometry to investigate the cooling and alteration history of the SJDD gabbro in order to decipher the main alteration process.

2. Geological background

2.1 Regional geology

The Armorican Massif is located in the western part of France, which was mainly assembled during to the Variscan orogeny. It formed during continental collision between Gondwana and Laurussia and the Ibero-Armorica microplate (Ballèvre et al., 2014; Martínez-Catalán et al., 2021). The collision began

during the Late Devonian and continued until the Early Carboniferous (Matte, 1986; Ballèvre et al., 2014; Martínez-Catalán et al., 2021). The Armorican Massif comprises three main domains (Fig. 1a) with contrasting structural styles and deformation histories: (i) the external, unthickened domain that consists of the Ibero-Armorica microplate, (ii) the Léon domain that corresponds to the Saxo-Thuringian zone and (iii) the South Armorican domain that corresponds to the deformed Gondwana margin. These domains are bound by two major dextral shear zones, the North Armorican Shear Zone and the South Armorican Shear Zone (NASZ and SASZ, respectively, in Fig. 1a). Located within the Ibero-Armorica plate, the North Armorican domain (NAD) constitutes an isolated fragment of the Pan-African belt that was structured during the Pan-African orogeny between 750 and 540 Ma and moderately affected by Variscan Carboniferous deformation. It generally constitutes a part of the upper, un-metamorphosed, brittle crust during the Variscan orogeny (Chantraine et al., 2001; Brun et al., 2001). According to Chantraine et al. (2001) and Ballèvre et al. (2001), the Cadomian orogeny started, between 620 and 600 Ma, at the Cadomian active margin with the building of a continental arc over a Paleo- to Neoproterozoic continental crust, related to a north-directed subduction. A back-arc extension lead to marginal rifting between 600 and 580 Ma. At the end of the subduction cycle, between 580 and 560 Ma, a strong shortening event was responsible for the basin inversion and a southward-directed general thrusting of volcanic and sedimentary units. Finally, partial melting and exhumation took place between 560 and 540 Ma. The end of the orogeny is recorded by an unconformity of Cambrian sediments on Cadomian granites and host rocks. Four contrasting diachronic units in the Pan-African block resulted from this orogeny (Figs. 1a and b), from west to east (Égal et al., 1996; Chantraine et al., 2001; Ballèvre et al., 2001): i) the Trégor-La Hague unit that contains remnants of a Paleoproterozoic crust (2000 Ma) intruded by granitoids at ca. 615 Ma; ii) the Saint-Brieuc unit, characterized by a thick 600 Ma-old volcano-sedimentary sequence deposited over a Neoproterozoic (750-650 Ma) basement, and intruded by 580 Ma-old gabbro and diorite; iii) the Saint-Malo unit, characterized by a thick detrital sedimentary unit highly metamorphosed up to partial melting; and iv) the Fougères unit, made of a thick and monotonous un-metamorphosed detrital sedimentary sequence intruded by numerous granites at ca 540 Ma. In this study, we focus on the Trégor-La Hague unit, which hosts the SJDD mafic complex (Figs 1b and 1c). From bottom to top, four main groups are recognized in this unit (Chantraine et al, 1985): i) the Paleoproterozoic Icartian orthogneisses; ii) the Neoproterozoic Brioverian group that includes several volcano-sedimentary, mafic lavas and detrital sedimentary formations; iii) the Silurian to Devonian sedimentary group, composed of alternating sandstone and shale formations, and iv) the Carboniferous Morlaix basin, made of Mississipian schists. These groups were mainly deformed by a Cadomian NW-SE compressive event leading to NE-SW isoclinal folding and associated schistosity cleavage with several SE-directed thrusts or reverse faults. The associated metamorphism is in-between the lower and upper greenschist facies. At the Devonian-Carboniferous boundary, a large mafic event occurred in the area, marked by the intrusion of thick dolerite sills and dykes (Barnénez in the west, Plestin in the east, Fig. 1c) and by the formation of the SJDD complex. The Variscan orogeny, which postdates this event, is marked by (i) a strong folding of all groups including the Carboniferous Morlaix basin, and (ii) a local overprint of the Cadomian metamorphism up to the amphibolite facies, in the east of the study area, transforming the Plestin dolerites into amphibolite and leading to lower

greenschist facies in the Carboniferous Morlaix basin. Finally, late Variscan granites intruded locally all older units.

2.2 The magmatic complex: structure and history

Several magmatic events occurred in the Armorican Variscan belt, with only one major mafic magmatic event close to the Devonian-Carboniferous boundary (Pochon et al., 2016b, 2018). This mafic event mainly formed a dense swarm of doleritic dykes and sills located in the external unthickened domain, intruding Late Proterozoic to Devonian sediments. Subsequent to this event, an isolated mafic body was emplaced within the unthickened NAD, the mafic-silicic intrusive complex of Saint-Jean-du-Doigt (SJDD).

The SJDD mafic-silicic complex is a heterogeneous, layered body that was emplaced at shallow crustal level (6–9 km, Barboni et al., 2011) within Paleoproterozoic to Carboniferous basement rocks. It displays textures of mingling and mixing between mafic and intermediate-felsic magmas (Caroff et al., 2011; Barboni et al., 2013). The SJDD mafic facies have tholeiitic to calk-alkaline affinities, which are interpreted as back-arc signatures. The SJDD pluton is made up of underplated subhorizontal sills with subordinate crosscutting dolerite dykes (Caroff et al. 2011, Barboni et al., 2013). Along the southwestern part, the SJDD pluton is bound by a normal fault, which brought it into contact with the Barnenez metadolerite (Fig. 1c). Field relationships indicate younging from east to west. Age dating (U-Pb) of single zircon by ID-TIMS confirmed this and corroborated that the SJDD was emplaced at 347 Ma, over a time span of 1.70 Ma (Barboni et al., 2013). Field relationships moreover show east-west variation in the degree of interaction between mafic and felsic magmas. In the east, stacks of bimodal sills show little interaction, whereas in the central and western parts, contacts between felsic and mafic sills show magma mingling. The sills show no significant post-emplacement, tectonic deformation. They have, however, undergone late to post-magmatic alteration, resulting in mineral-scale replacement reactions without significant change in the bulk chemistry (Caroff et al., 2011). Along the shoreline, the SJDD pluton is exposed along a continuous cross-section that has been divided into three main zones from east to west. According to the field observations and characterization of Caroff et al. (2011) and Barboni et al. (2013), a brief description of each zones is summarized as follows.

The first zone is exposed at the Poul Rodou locality in the east and is composed mainly of interlayered bimodal sills of gabbroic and granitic rocks. Indeed, several sub-parallel granitic sheets consist of layers within the gabbroic body. The thickness of granitic layers ranges between few up to several decimeters. The spacing from one granitic layer to another varies from meters to ten meters, and layers are sometimes connected by irregular dykes. Diapirs, lobate and sharp contacts between the granite and the gabbro indicate magma mingling during contemporaneous emplacement (Supplementary material 1a and b). In the current orientation, the sills have variable dipping angles, but show overall northeastward tilting.

The second zone is exposed at the Saint-Jean-du-Doigt seashore and corresponds to the central part of the pluton. This zone shows two spectacular records of interactions between gabbroic and granitic rocks that are distinct on both sides of a dextral fault (Fig. 1c). Brittle brecciation predominates eastward,

whereas mingling and mixing predominate westward. To the east, the angular breccias consist of jigsaw-type, where gabbro is enclosed in vein networks of tonalite and granodiorite compositions (Supplementary material 1c). To the west, mingling and mixing suggest ductile interactions between coexisting mafic and felsic magmas. Some partly hybridized facies can be observed. Subvertical layering of bimodal dyke swarms associated with flow-banding structures suggest multiple, near-contemporaneous vertical injections of magma within feeder zones.

The third zone is located in the western part of the pluton. It consists of a pegmatoid-cumulate association within gabbro. Cumulates form small lenses comprising mm- to cm-scale plagioclase, amphibole and Fe-Ti oxides within gabbro. The pegmatoids form pods or veins with variable, cm-scale plagioclase, and amphibole and Fe-Ti oxides within the main gabbro and are sometimes associated with aplite (Supplementary material 1d). They appear to be late, because they crosscut the gabbroic assemblage along straight contacts.

The structure and assembly of the SJDD pluton remains debated. Earlier models (Caroff et al., 2011) have suggested that the pluton resulted from in-situ crystallization of a relatively uniform magma reservoir, in which the eastern part represents the lower levels of the intrusion, while later models (Barboni et al., 2013) have inferred that the pluton was built by numerous sill injections. Barboni et al. (2013) also concluded that the eastern part of the pluton corresponds to the intrusion roof, on the basis of the observation of roof-contact host rocks.

3. Samples and methods

Reconstructing the current 3D geometry of the SJDD intrusion is the best way to give an overview of its orientation, direction and thickness as well as the location of the intrusion roof. For this purpose, we used the 3D Geomodeller ® software package version 4.0.7 (BRGM–Intrepid Geophysics; http://www.geomodeller.com, Lajaunie et al., 1997; Calcagno et al., 2008). A detailed description of the 3D modelling method can be found in Supplementary material 2.

Among samples collected along the shoreline, six gabbroic samples were selected as representative from the three main zones: samples 022 and 018 for the western part, samples 011 and 014 for the central part, and samples 003 and 006 for the eastern part (Fig. 2). We have collected only samples with gabbroic facies devoid of mixing or hybridization textures. These selected samples were crushed and powdered using agate mortars. Major and trace element analyses, including REE analysis, were performed by ALS Global Ltd. Laboratories (Loughrea, Ireland) using their CCP-PKG01 package. The data are provided as part of Supplementary material 3.

Textural observations and chemical analyses were performed on thin sections for amphibole, clinopyroxene and apatite and on polished epoxy resin blocks for Ti-minerals. Mineral separation procedures were applied to concentrate the Ti-minerals. Rocks were crushed and heavy minerals were concentrated from the < 400 µm powder fraction using a Wilfley table and heavy liquids. Magnetic minerals were then removed with a hand magnet. Grains were carefully handpicked under a binocular microscope and embedded in epoxy mounts. The grains were successively ground and polished on a

lap wheel using 9 to 1 µm diamond suspensions. Mounted grains were then imaged by a Merlin Compact ZEISS scanning electron microscope (SEM) equipped with a GEMINI I column.

Quantitative analyses and X-ray chemical maps were acquired using a Cameca SX-Five electron probe micro-analyzer (EPMA) at the ISTO-BRGM laboratory (Orléans, France). Amphibole, clinopyroxene, plagioclase, titanite, ilmenite and TiO_2 polymorphs were analyzed. Analyses were performed at an accelerating voltage of 15 kV, a beam current of 10 nA, and with a focused beam, using the following mineral standards: albite (Si*Kα,* Na*Kα*), Al_2O_3 (Al*Kα*), hematite (Fe*Kα*), MgO (Mg*Kα*), pyrophanite (Ti*Kα*, Mn*Kα*), apatite (P*Kα*), topaz (F*Kα*), andradite (Ca*Kα*), orthoclase (K*Kα*), vanadinite (V*Kα* , Cl*Kα*), NiO (Ni*Kα*), Cr_2O_3 (Cr*Kα*), ZnO (Zn*Kα*) and zircon (Zr*Kα*). Analyzed elements, detailed lists and detection limits can be found in Supplementary material 4. For ilmenite and clinopyroxene, the Fe^{3+} content was calculated using the method described by Droop (1987). For amphibole, structural formula were calculated using the method described in Ridolfi et al. (2018).

Trace element concentrations were determined in situ by laser ablation inductively coupled plasma mass spectrometry (LA-ICP-MS) at ISTO for amphibole, clinopyroxene, ilmenite, titanite and TiO_2 polymorphs. The system consists of a RESOlution-SE (ASI) 193 nm excimer laser with an S155 ablation cell (Laurin Technic) coupled to an Agilent 8900 QQQ inductively coupled plasma quadrupole mass spectrometer (LA-ICP-MS). Ablation was carried out using a He carrier gas, mixed with Ar as a cell and nebulizer gas. Calibration was performed before each analytical session on NIST SRM 612 reference glass minimizing U/Th fractionation (~ 0.998 %) and the production of oxides (ThO^+/Th^+ ~ 0.116 %) and doubly charged ions (Ca^{2+}/Ca^+ ~ 0.210). Laser beam size (20-30 µm), repetition rate (3-7 Hz) and the on sample fluence (~3-4 J/cm^2) were varied for the different analyzed minerals. A SQUID device was used to smooth out ablation signal fluctuations for analyses at low (<7 Hz) laser repetition rates. The list of analyzed elements is summarized in Supplementary material 5 together with details of the instrumentation and analytical conditions. Ablation areas were carefully selected to avoid ablating micro-inclusions, except for ilmenite for which analyses aimed at characterizing the composition of micro-inclusions. Single analysis consisted of 30 s of background collection followed by 40 s of ablation and 15 s and wash-out delay. For each analytical session, about 2-5 reference materials were analyzed before and after each set of 12-15 sample analyses, following classical bracketing procedure. For ilmenite, titanite and TiO_2 polymorphs, the internal standard used was ^{47}Ti, whereas GSE-2g was used as the primary reference material. The NIST610 and BCR-2g reference material measurements were treated as unknowns and used to control reproducibility and accuracy of the analyses. For amphibole and clinopyroxene, the internal standard used was ^{43}Ca, whereas NIST610 was used as the primary reference material. The NIST612 and BCR-2g glass standard measurements were treated as unknowns and used to monitor the quality of analyses. Data reduction was carried out using the data reduction scheme Trace_Elements_IS, a set of Igor Pro procedures that work with the Iolite 2.5 software (Paton et al., 2011). We have excluded approximately the first ~ 5 s of the integration signal from our data reduction because the ablation impact causes artificially high concentration peaks.

4. Results

4.1 3D implicit geological modeling of the SJDD intrusion

The interpolated Bouguer anomaly map of the study area shows two main anomalies (Supplementary material 2a): a positive anomaly towards the SE of the mapped intrusion ranging from 6 to 11.43 mGal and a negative anomaly towards the NW of the mapped intrusion ranging from -3 to 0 mGal. Because of the known high density of mafic rocks, the positive anomaly is surely related to the presence of the SJDD gabbro intrusive complex. Consequently, inverse 3D geological modelling of gabbro is facilitated because of the significant density contrast between gabbro and its country rocks. Dolerite and amphibolite have densities close to gabbro, but their small size does not significantly affect the result of the modelling. Taking into account the geophysical data (interpolated Bouguer anomaly) and all geological data (cross section, cleavage, bedding, and geological contacts), the result of the iterative 3D modelling yields a sill-like geometry dipping to the SE for the SJDD gabbro (Fig. 2 & Supplementary material 2c). The long axis appears to be NW-SE with a root located to the SE. The root of the SJDD mafic body seems to be anchored at least up to a 6 km depth. The generally good agreement between the gravity anomaly generated by the 2D cross-sections and the measured gravity anomaly constitutes a validation of the overall 3D geometry of the SJDD intrusion (two examples are given in the Supplementary material 2b). The thickness of the mafic body varies from 0.2 to 3.2 km, with ~ 1.2 km thick below Poul Rodou (eastern part), ~ 0.6 km below SJDD seashore (central part) and ~ 0.3 km below Primel (western part). Thus, due to surface erosion and tilting, this intrusion displays a full and well-exposed cross-section from its top at in the east to its bottom in the west of the shoreline.

4.2 Whole-rock compositions

Whole rock data can be found in Supplementary material 3. In a total alkali silica (TAS) diagram (Fig. 3a), all the samples from the three main zones display gabbroic affinities. The alkali content (Na_2O + K_2O) slightly differs between different zones. An increase of the K_2O content can be observed from west to east with mean values of 0.42 wt.%, 0.50 wt.% and 1.16 wt.% K_2O in the three zones (see inset in Fig. 3a).

To estimate the degree of alkali mobility during possible metamorphic or hydrothermal alteration, our new and published data for SJDD (Coint et al., 2008; Caroff et al., 2011) are plotted in the K_2O+Na_2O vs. $K_2O/(K_2O+Na_2O)$ diagram (Hughes, 1973; Fig. 3b) and in the chlorite-carbonate-pyrite index (CCPI) vs. Ishikawa alteration index (AI) diagram (Large et al., 2001; Fig. 3c). In these diagrams, we also plotted the compositions of dolerites strongly affected by hydrothermal alteration (Pochon, 2017; Pochon et al., 2016b, 2018), hornblende gabbros that underwent autometasomatic alteration (Pe-Piper et al., 2010) and gabbros of the Chenaillet Ophiolite altered by seawater or albititic melt (Tribuzio et al., 2019; Nicollet et al., 2022) in order to illustrate the effect of several types of alteration of mafic rocks. Most of the SJDD samples fall within the igneous field; samples from the eastern part, in particular, fit well with the field of the autometasomatised hornblende gabbros, which mostly overlaps the igneous field (Figs. 3b and c). This suggests that no significant element mobility (i.e. of major elements) has occurred after magmatic crystallization.

Chondrite-normalized REE patterns of the SJDD gabbro are plotted in Fig. 3d. Except for sample 022, all studied samples display light REE (LREE) enrichment with moderate fractionation of middle-REEs (MREEs) and heavy-REEs (HREEs). The patterns are similar to those of enriched mid-ocean ridge basalts (E-MORB). Light REE enrichment (including data from the literature) for the western, central and eastern part range from 30 to 285, 35 to 300 and 110 to 320 times the chondritic abundance.

4.3. Textural relations and mineral compositions

As previously described, the SJDD gabbro mainly consists of three main zones along the SE-NW cross-section. The detailed textural and mineralogical observations reveal an alteration gradient from the lower (western) to the upper (eastern) parts. A summary of the mineralogical description of samples can be found in Table 1.

4.3.1 Plagioclase

In the whole intrusion, plagioclase shows no alignment and most primary crystals show no or little zoning. Plagioclase in the lower (western) part of the intrusion is largely unaltered, except for rim corrosion by clinopyroxene and amphibole (Figs. 4a-c). Plagioclase size ranges from 80 to 600 µm. In the central part of the intrusion, plagioclase crystals are tabular, larger in size (150 µm to 1.5 mm), and partially corroded by amphibole (Figs. 4c and d). The main difference relative to the western part is that the crystals underwent partial saussuritization (i.e. alteration of plagioclase to zoisite and sericite) with saussuritization tending to be more significant in the crystal cores (Fig. 4d). In the eastern part of the intrusion, plagioclase grains are tabular and up to 0.5 to 1 mm in size, and they are strongly to completely saussuritized (Figs. 4e and f). The progressive alteration of plagioclase from the lower to the upper part of the intrusion (western to the eastern part) is accompanied by a progressive change in the chemistry of the plagioclase: Ca-rich plagioclase (An50 - labradorite) dominates in the lower part (western zone), Ca-rich to Na-rich plagioclase (An20-42 – andesine to oligoclase) in the central zone, and Na-rich plagioclase (An2 - albite) in the upper part (eastern zone) (Supplementary material 6).

4.3.2 Clinopyroxene

No clinopyroxene crystals were observed in the lower part of the intrusion (eastern zone). They are scarce in the central part, and relatively rare in the upper (western) part. Clinopyroxene is generally subhedral. It is smaller in the western part (mean size of 100 µm, Fig. 4b), relative to the central part (mean size of 600 µm, Fig. 4f). All clinopyroxene crystals are partially replaced by actinolite along crystal rims and microcracks, with actinolite thickness varying between 5 and 100 µm (Fig. 4f). Clinopyroxene is mainly diopside, with a mean wollastonite content of 45 %. $Mg/(Mg+Fe^{2+})$ is always close to 0.85, and Na and Ti contents are always low, around 0.2 atoms per unit formula (apfu). The only compositional difference between clinopyroxene from the western and the central part is their Al content, on average 0.07 and 0.12 apfu, respectively (Supplementary material 4).

4.3.3 Amphibole

The complete dataset of amphibole analyses is available in Supplementary material 4, in which amphibole compositions were classified according to Hawthorne et al. (2012). However, throughout text and figures, we use a simplified classification (Santos et al., 2020): brown and dark green amphiboles, with composition ranging from pargasite to magnesio-hastingsite, are referred to as brown magnesio-hastingsite and dark green pargasite (depending on their color), whereas green and colorless amphiboles are referred to as magnesio-hornblende and actinolite, respectively. Pale green amphiboles are referred to as actinolitic hornblende, a transitional amphibole between magnesio-hornblende and actinolite.

In the lower (western) and central parts of the intrusion, four types of amphibole are observed. Actinolite is the most common type and frequently hosts (i) fluid inclusions oriented along planes, intersecting at 90°, Fig. 4b), and (ii) solid inclusions of sulfides (pyrrhotite and chalcopyrite) within the crystal cores (Fig. 4c). Actinolite rims clinopyroxene and magnesio-hornblende and is frequently enclosed by dark green pargasite, but can also be found directly in contact with fresh plagioclase (Figs. 4a-c). Dark green pargasite may also form needles overgrowing actinolite and radiating into plagioclase. Magnesio-hornblende is rare in the western part, whereas it is frequent in the central part. It forms subhedral crystals, intergrown with and commonly enclosing subhedral-euhedral plagioclase (Fig. 4e). Brown magnesio-hastingsite is the rarest amphibole type within the western and the central parts. It forms irregular cores in magnesio-hornblende. In the eastern part, only three types of amphibole are present (Figs. 4g-i). Dark green pargasite is not observed. Well-preserved, euhedral brown magnesio-hastingsite is typically rimmed by magnesio-hornblende, which is crosscut by actinolite (Fig. 4i). The contacts between magnesio-hastingsite and magnesio-hornblende are sharp and straight, while those between actinolite and the other two amphibole types are sharp and irregular. Note that actinolite is frequently associated with quartz and epidote (Figs. 4g and h).

All amphiboles are calcic (see Fig. 5 and Supplementary material 4). Analyses with Al_{tot} below 0.75 apfu (calculated on a 23-oxygen basis) are considered as secondary alteration products (Lewis et al., 2021). Actinolite has low Al_{tot} values ranging between 0 and 0.5 apfu (mean value of 0.3 apfu), and low Ti values between 0 and 0.26 apfu (mean value of 0.02 apfu). Actinolite has the highest molar Mg# values between 54 and 76 (mean value of 68). Magnesio-hornblende is slightly more enriched in Al, Ti and Fe than actinolite, with Al_{tot} values ranging between 0.7 and 1.2 apfu (mean value of 0.9 apfu), Ti values between 0.08 and 0.19 apfu (mean value of 0.13 apfu) and Mg# values between 54 and 69 (mean value of 63). Actinolitic hornblende is characterized by intermediate values relative to actinolite and magnesio-hornblende, with Al_{tot} mean value of 0.44 apfu, mean Ti value of 0.04 and mean Mg# of 62. Compared to actinolite and magnesio-hornblende, dark green pargasite has more variable composition with high Al_{tot} values between 0.9 and 3.0 apfu (mean value of 2.1), low Ti ratios between 0 and 0.3 (mean value of 0.1), and Mg# values between 36 and 64 (mean value of 48). Finally, brown magnesio-hastingsite stands out from the rest of the amphibole types as it has the highest Ti values, which are between 0.16 and 0.39 (mean value of 0.31). The main differences between amphibole compositions in the western and the eastern part of the intrusion can be seen in the Fig. 5. In the western part, amphibole compositions form a continuous, negatively correlated trend for Al_{tot} and Mg#

(especially dark green pargasite) and almost no correlation for Ti and Al_{tot} In the eastern part (Figs. 5e and f), amphibole composition shows a negative correlation between Al_{tot} and Mg# and between Ti and Al_{tot}, however, it does not define a continuous trend but rather three distinct compositional clusters. Amphibole compositions from the central part are intermediate to those of the western and eastern parts (Figs. 5c and d).

Brown magnesio-hastingsite is generally more enriched in trace elements, and particularly in the REEs, than other amphiboles, followed by magnesio-hornblende, actinolite and dark green pargasite (Figs. 6a-c). In the eastern part, the REE patterns of the three types of amphibole are similar, showing slightly positively sloped LREE segments and flat MREE to HREEs segments with negative Eu anomalies. In the western part, the REE pattern of brown magnesio-hastingsite is similar, but those for actinolite and dark green pargasite differ. The actinolite REE pattern is similar to that of clinopyroxene and dark green pargasite. In addition, dark green pargasite displays a positive Eu anomaly (Fig. 6a). For the other analyzed trace elements (Figs. 6d-f), the spectra of the different amphibole types are equally similar for the eastern part, whereas those of the western and central parts are more variable. However, amphibole in the eastern part shows a clear positive Nb-Ta anomaly, whereas it shows a positive Li anomaly in the western and central parts. Dark green pargasite displays the highest Li values (between 2.4 and 28.0 ppm, mean value of 8.9 ppm). As for the REEs, the concentrations of other analyzed trace elements in actinolite are similar to those of clinopyroxene in the western part, whereas they are similar to the magnesio-hornblende in the central and eastern part (Figs. 6d-f).

4.3.4 Ilmenite and associated Ti-rich minerals

Within the three zones, ilmenite crystals are subhedral to anhedral (Fig. 7). They occur along grain boundaries between plagioclase and amphibole, or between plagioclase and clinopyroxene, or between amphibole crystals (e.g. between brown magnesio-hastingsite and magnesio-hornblende, or between actinolite cores and dark green pargasite rims). Ilmenite can thus be found in direct contact with almost all major minerals. No titanomagnetite or hematite exsolution textures have been observed (Fig. 7a), except within cumulate facies (sample 018) in the western part, which show characteristic trellis-like exsolution lamellae of ilmenite within magnetite. In the central and eastern parts, ilmenite hosts a high density of crystal defects, which consist of vacancy aggregates (i.e. voids; Figs. 7b-d). As voids are generally caused by gases that are trapped during crystal growth, voids will be referred to as fluid inclusions (FIs) for more clarity in the rest of the paper. This shortcut will be discussed in detail later in the paper. In the central and eastern parts, fluid inclusions show either negative crystal (Figs. 7e and f) or irregular shape (Fig. 7i) with sizes ranging between 0.5 and 5 µm. In the lower (western) part of the intrusion (gabbro and cumulate facies), only FI-free ilmenite is observed. Ilmenite of the central and eastern part of the intrusion is locally extremely rich in FIs (FI-rich ilmenite) and elsewhere devoid of FIs (FI-poor ilmenite). FIs are commonly arranged in sub-parallel trails, which occur parallel to the elongation (i.e. the c-axis) of the ilmenite (Figs. 7c and f), but some FI trails are randomly oriented, possibly following healed micro cracks. FI-rich zones mostly occur in the cores of crystals, whereas the FI-poor zones typically form rims (Figs. 7c and d). However, FI-poor zones are also observed along

micro cracks in some crystal cores (Fig. 7h) or sometimes without preferred orientation (Fig. 7d). Ilmenite crystals from the upper (eastern) part of the intrusion are mostly FI-rich; these FIs are smaller and more concentrated than in crystals from the central part, attaining up to 15 % of the total crystal surface. Numerous nm-sized solid inclusions can also be observed in the ilmenite crystals, mainly consisting of baddeleyite (Fig. 7i) and, to a lesser extent, of sphalerite and pyrite. In the eastern part of the intrusion, ilmenite is rimmed by titanite (Figs. 7c, d, g and h), the contact between the two phases being sharp and irregular. Titanite generally forms a ~ 10 µm-thick rim around ilmenite, but may spread deeper toward the ilmenite core (Fig. 7g). It is also associated with a TiO_2 polymorph that was identified as a rutile using Raman spectroscopy (Supplementary material 7). Rutile forms blocky crystals (~20-40 µm in size) with more or less uniform crystallographic orientation and it is associated with voids classically related to the replacement of ilmenite by rutile (Putnis, 2009). Textural relationships suggest that titanite crystallized before rutile. Zircon is often present at the margins of the primary ilmenite crystals or in fractures (Fig. 7h)

Inclusion-rich and inclusion-poor ilmenite compositions belong to the Fe^{2+} and Ti end-members of the true ilmenite-hematite solid solution. A progressive increase in calculated Fe^{2+} and Mn^{2+} and Ti contents (Fig. 8a) and a progressive decrease of calculated Fe^{3+} content (Fig. 8b) is observed from the lower (western) to the upper (eastern) part of the intrusion. The FI-poor and the FI-rich ilmenite zones show no compositional differences in major and minor elements (Fig. 9). A slight difference in Ti concentration can be observed, which likely results from the high abundance of FIs (i.e. Ti is known to be incompatible in fluids, Klemme et al. 2006). Titanite is homogeneous in Ca, Fe, Ti, Si and Al (Fig. 9).

The concentration of trace elements in ilmenite are plotted as univariate boxplot diagrams (Figs. 8c and d). The complete dataset is provided in Supplementary material 8. Si, Co, Ni, Cu, and Hf have similar concentrations in all ilmenite types. On the contrary, Sr, Y, Nb, Ta, Mo, Sn, Sb, W, and Pb are generally enriched in FI-bearing ilmenite (Fig. 8c). The most striking observation is that Mo, Sn, Sb, W, Pb, and, to a lesser extent Sr and Nb, show a progressive enrichment from FI-free over FI-poor to FI-rich ilmenite. For example, FI-free ilmenite has a median Sb value of 0.4 ppm, whereas FI-poor and FI-rich ilmenite have median Sb values of 0.7 and 1.6 ppm, respectively. Similar enrichment is observed for ∑(Mo+Sn+Sb+W+Pb), clearly showing a progressive increase of median concentration values from 2.7 over 14.7 to 25.5 ppm for FI-free, FI-poor and FI-rich ilmenite, respectively. This implies a progressive enrichment of these elements in the ilmenite from the lower to the upper part of the intrusion (western to eastern zones; Fig. 8d).

5. Discussion

5.1 Estimation of equilibrium crystallization temperatures

Crystallization temperature estimates were calculated by applying several geothermometers (Fig. 10). We used the Al-in clinopyroxene-only thermometer from France et al. (2010), the Ti-in amphibole-only thermometer from Liao et al. (2021), the Zr-in titanite-only thermometer from Hayden et al. (2008) and the Zr-in rutile-only thermometer from Kohn (2020). The use of geothermometers needs a rigorous check of their applicability. For example, the Al-in clinopyroxene thermometer (France et al., 2010) was

calibrated for mafic root zones of sheeted dike complexes. The Al_2O_3 content in clinopyroxene is strongly temperature-dependent, but, because it is also dependent on pressure, this thermometer is only restricted to low pressures, which is the case for the SJDD gabbro (Barboni et al., 2011). Like clinopyroxene, amphibole is widely used to infer magmatic crystallization temperatures (Holland and Blundy, 1994; Ridolfi et al., 2010; Ridolfi and Renzulli, 2012; Putirka 2016). One of the most used thermometers is the classical amphibole-plagioclase thermometer of Holland and Blundy (1994) calibrated for the Si-Na-Al-Ca composition of equilibrium pairs. However, it implies that amphibole and plagioclase are in compositional equilibrium, which is not easy to assess in our case, and consequently the use of this thermometer needs care (Blundy and Cashman, 2008), especially when rocks underwent intense heterogeneous alteration overprint, as in the case of the SJDD gabbro. Amphibole-only multi-component thermometers were developed (Ridolfi et al., 2010; Ridolfi and Renzulli, 2012; Putirka 2016) and successfully applied to igneous systems, but have unpredictable uncertainties for slowly-cooled rocks (Liao et al., 2021) and are not calibrated for subalkaline systems. However, several authors have proposed a Ti-in-amphibole thermometer (Otten, 1984; Liao et al., 2021), as Ti content in amphibole is temperature-dependent (Raase, 1974). It was calibrated for a wide range of temperatures (i.e. between ~400 and 1000°C, Liao et al., 2021) and requires a Ti-buffer mineral such as ilmenite, titanite or rutile. This thermometer is applicable to the SJDD gabbro, because it is suitable for subalkaline mafic systems over a large range of temperatures. The titanite thermometer is based on Zr incorporation into titanite that strongly increases with temperature, and was calibrated by experiments involving natural titanite, in the presence of quartz and rutile over a temperature range of 600-1000°C (Hayden et al., 2008). This thermometer is particularly suited for the SJDD gabbro, which contains a significant proportion of rutile and some quartz in the interstices (Figs. 4g, 4h and 7g). Similarly to titanite, the Zr content of rutile is sensitive to temperature (Zack et al., 2004; Tomkins et al., 2007; Kohn 2020). The Zr-in-rutile thermometer of Kohn (2020) was calibrated for a temperature range of ~400-1400°C, which is thus applicable in our case, as rutile appears to co-crystallize with zircon and quartz during ilmenite breakdown, which is a condition for applying this thermometer. For the Zr-in titanite and rutile thermometers, we used a lithostatic pressure of 200 MPa, which is consistent with a shallow depth of gabbro emplacement in the crust.

Estimated temperatures (Fig. 10) are in agreement with the paragenetic sequence estimated on the basis of textural relationships and compositional variations. Clinopyroxene gives the highest temperatures with mean values around 986 ± 40°C (uncertainty of thermometer given by France et al., 2010). For amphibole, decreasing temperatures are consistent with the color change from brown to green, which qualitatively reflect the Ti content (Nicollet et al., 2022). Brown magnesio-hastingsite gives high temperatures with mean values around 909 ± 35°C (uncertainty of thermometer given by Liao et al., 2021). Magnesio-hornblende yield a range of temperatures with a mean value around 719 ± 35°C, whereas actinolitic hornblende and actinolite yield a more dispersed range of temperatures with a mean value around 542 ± 35°C and 462 ± 35°C, respectively. Although dark green pargasite rims surround actinolite cores, it yields temperatures more elevated than actinolite around 552 ± 35°C, consistent with its darker green color. Crystallization temperatures of titanite and rutile are also in complete agreement with their stability field (Jamieson and Olinger, 1969; Liou et al., 1998): titanite yields higher

temperatures than rutile with a mean value around 668 ± 20°C (uncertainty of thermometer given by Hayden et al., 2008), whereas rutile yields a mean value of 593 ± 15°C (uncertainty of thermometer given by Kohn, 2020).

5.2 Amphibole record of cooling

The SJDD gabbro hosts a large quantity of calcium amphibole as phenocrysts in interstices, which raises questions regarding its magmatic or metamorphic origin. The common textural relationship between the various amphibole types is that brown magnesio-hastingsite is always overgrown by magnesio-hornblende and sometimes by actinolite (Fig. 4i). A crystallization sequence from brown magnesio-hastingsite to magnesio-hornblende to actinolite is observed in agreement with estimated temperature. In the eastern part, amphibole compositions (Fig. 5) show a discontinuous compositional cluster between brown magnesio-hastingsite and magnesio-hornblende. The first has high Ti content and intermediate Al content, while the second has low Ti and Al content. The two distinct compositional populations do not define a continuous trend of decreasing Al with increasing Mg# in the eastern part (Fig. 5f), indicating that mineral compositions of brown magnesio-hastingsite and magnesio-hornblende were not significantly affected by secondary subsolidus chemical exchange (Lewis et al., 2021). This also indicates that the estimated temperatures of 833°C and 719°C are well representative of the crystallization conditions of brown magnesio-hastingsite and magnesio-hornblende, respectively. This interpretation is consistent with the fact that brown magnesio-hastingsite is also the most enriched in REE and HFSEs (Figs. 6a-c). In the western part, brown magnesio-hastingsite has similar values of Ti and Al, with Ti contents slightly lower and Al contents slightly higher than in the eastern part, probably representing preserved magmatic amphibole. Furthermore, the relatively high Ti content of brown magnesio-hastingsite probably indicates that it crystallized before the appearance of ilmenite (i.e. the main Ti-carrier in mafic rocks), whereas the lower Ti content of magnesio-hornblende and estimated temperatures may suggest that it crystallized after ilmenite. Thus, we interpret brown magnesio-hastingsite as a primary magmatic amphibole and the magnesio-hornblende as amphibole crystallized at the magmatic-hydrothermal transition.

In addition, actinolitic hornblende, actinolite and dark green pargasite also crystallized at lower temperatures. On the basis of textural relationships, mineral compositions and estimated temperatures, several processes have been identified to explain the origin of these amphiboles. The very low content of Ti and Al indicates that actinolite and actinolitic hornblende are secondary amphiboles of metamorphic and/or hydrothermal origin (Lewis et al., 2021). In the western part, the actinolite (and actinolitic hornblende) pseudomorphs after clinopyroxene preserve the former shape and the oriented cleavage of clinopyroxene (Figs. 4b and c). This suggests, together with the similar REE spectra shape of clinopyroxene and actinolite (Figs. 6a-c), that actinolite and actinolitic hornblende mainly derive from clinopyroxene. However, we cannot exclude that some actinolite formed by decomposition of primary amphibole. At the opposite, the progressive replacement of brown magnesio-hastingsite and magnesio-hornblende by actinolite and/or actinolitic hornblende (Figs. 4h and i), and their similar REE spectra shape (Figs. 6a-c) rather suggest that in the eastern part, actinolite derives from the destabilization of

primary amphiboles. Again, we cannot exclude that some actinolite derives from clinopyroxene in the eastern part, although we have never observed clinopyroxene in this area. The difference in the origin of actinolite may be explained by the fact that clinopyroxene is likely to have been the dominant Mg phase in the western part, whereas amphibole predominated at the intrusion roof, due to a higher volatile content . Concerning the central part of the intrusion, the two types of actinolite are observed (Figs. 5c and d), suggesting that amphibole occurrence increases progressively from the lower part to the intrusion roof.

Regarding the dark green pargasite (common in the lower part but absent in the intrusion roof), its origin seems to be distinct and later than actinolite, as it overgrows pseudomorphs of actinolite. Furthermore, it seems that dark green pargasite results from an increase in temperature of the system, as it yielded higher estimated crystallization temperatures than actinolite (i.e. ~ 552°C). This could be related to either metamorphic (e.g. slow diffusion), magmatic (e.g. interaction with residual hydrous melt), or hydrothermal events (e.g. percolation of hot fluids into grain boundary). We interpret the growth of dark green pargasite as a fluid-assisted metamorphic event, which occurred after the solidification of the gabbro: the dissolution of actinolite and plagioclase resulted in the precipitation of dark green pargasite. The temperature increase and the fluid percolation may derive from the late emplacement of mafic pegmatite dykes or late granite intrusions, which are observed in the lower and central parts of the intrusion, but details of the proposed interpretation need further investigation.

5.3 Ilmenite as a surprising trap of magmatic fluids

Since section 4.3.4, we have referred to voids in ilmenites as fluid inclusions, which needs to be discussed before further interpretation. What we observe at the exposed crystal surface of ilmenite are not inclusions (Figs. 7b-i) but empty holes that we call voids. There are three main possibilities to explain the formations of these voids: (i) damage caused by polishing, (ii) former melt inclusions or (iii) former fluid inclusions. Because abrasive defects would not have a strong crystallographic control and because the voids are empty, the observed voids cannot originate from damage caused by polishing or from trapped melt inclusions. In conclusion, voids can only be former fluid inclusions that were purged and leaked during polishing. In addition, the strong crystallographic control and the orientation of the voids are strong arguments for the fluid inclusion hypothesis. Ilmenite crystals of the central and upper parts of the intrusion show respectively high and extremely high abundance of fluid inclusions, whereas they are inclusion-free in the lower part of the intrusion. LA-ICP-MS analyses reveal that FI-bearing ilmenite is enriched in Sr, Y, Nb, Ta, Mo, Sn, Sb, W and Pb, with respect to FI-free ilmenite. In particular, Mo, Sn, Sb, W and Pb show a progressive enrichment from FI-free to FI-rich ilmenite, through FI-poor ilmenite (Fig. 8c). This suggests that these strongly incompatible elements (Klemme et al. 2006) are concentrated in the fluid inclusions and explains why ilmenite is enriched in Mo, Sn, Sb, W and Pb from the lower to the upper part of the intrusion (Fig. 8d).

Based on textural relationships, two types of intra-crystal FI trails were identified: (i) well-arranged and (ii) randomly oriented FI trails that may crosscut well-arranged trails. The occurrence of two types of FIs hints at several episodes of fluid trapping, whereas the negative shape and the small size of the

inclusions suggest that both FI trails underwent post-entrapment processes such as necking down (Bodnar, 2003). A strong crystallographic control can be inferred for the well-arranged FI trails from the orientation along the same preferential direction within the same crystal (Figs. 7c, d, f, g and h), and the negative crystal shape of the FIs (Figs. 7e and f). The parallel planes identified by the well-arranged FI trails may not be considered as cleavage planes, because ilmenite has none (Wechsler and Prewitt, 1984). We interpret them as resulting from either primary processes such as the formation along growth zone planes or growth twins, or secondary process such as microcracking, mechanical twinning, or dislocation creep. All FI trails formed before ilmenite breakdown to titanite and rutile, because titanite and rutile are devoid of FIs and are always in contact with a FI-free ilmenite rim (Figs. 7c, d, g and h). Our textural observations and chemical analyses are consistent with the breakdown of ilmenite via interface-coupled dissolution-reprecipitation. The lobate contact between ilmenite and titanite (Figs. 7c, d, g and h), the preserved shape of ilmenite, and the occurrence of rutile-filled cracks highlight fluid pathways, in agreement with the numerous natural and experimental studies showing that the recrystallization of ilmenite to titanite and rutile occurs via pseudomorphic replacement (Janssen et al., 2010; Angiboust and Harlov, 2017; Pochon et al., 2017). The coexistence of titanite and rutile indicates a physical-chemical switch in the system at a given time, resulting in the appearance of rutile in place of titanite. This change is consistent with the temperature decrease recorded by the incorporation of Zr into titanite and rutile from 679 to 593°C (Fig. 10). Rutile-titanite stability is strongly influenced by Ca activity in the system: when Ca is available, titanite crystallization is favored (Angiboust and Harlov, 2017). Thus, we propose that (i) ilmenite breakdown is the result of fluid-assisted dissolution-precipitation replacement at relatively high temperature, (ii) the crystallization of titanite occurred at Ca-rich conditions, due to the concomitant saussuritization, and (iii) the appearance of rutile in place of titanite reflects a decrease of temperature and Ca availability, probably due to the crystallization of epidote and apatite. We also propose that ilmenite breakdown occurred after FI entrapment, concurrently with plagioclase alteration and magnesio-hornblende crystallization, at temperatures between 700 and 600°C, during pluton cooling at fluid-present conditions

As FI entrapment seems to precede ilmenite breakdown, we propose that FIs are either primary, i.e., they formed during magmatic crystallization of ilmenite, or pseudo-secondary, i.e., they result from micro-cracking during plastic deformation of ilmenite after its crystallization. We favor the first hypothesis for two reasons: (i) if FI trails were healed fractures produced by crack-seal process, they would be restricted to extensional veins (i.e. brittle conditions) and such veins should also be present in other mineral phases, such as primary plagioclase or clinopyroxene, which is, however, not the case; (ii) fluids entrapped in the inclusions seem to be in equilibrium with ilmenite, as FI-bearing zones have the same major element composition of FI-free zones (e.g. Figs. 8 and 9), whereas the occurrence of titanite and rutile clearly speaks for a later destabilization of ilmenite, as also observed in the literature (Pochon et al., 2017; Pearce et al., 2021). In addition, the occurrence of small, randomly oriented baddeleyite inclusions in ilmenite (Fig. 7i) suggests a synchronous crystallization of the two phases (Beckman and Möller, 2018). On the contrary, zircon crystals occur in fractures, or at the crystal boundaries, associated with titanite and rutile (Fig. 7h), suggesting that baddeleyite inclusions are dissolved during the replacement reaction and redeposited as zircon grains. The presence of numerous

baddeleyite inclusions in the FI-rich ilmenite cores therefore suggests that FI entrapment occurred during magmatic crystallization of ilmenite. We therefore propose that FIs may have trapped magmatic fluids coexisting with ilmenite during its late magmatic crystallization. Late magmatic fluids are typically enriched in Mo, Sn, Sb, W and Pb; and these elements are therefore typically enriched in magmatic fluid inclusions (e.g., Zajacz et al., 2008; Fulignati et al., 2011), and volcanic gases (e.g., Allard et al., 2000; Henley and Berger, 2013). The presence of such metals in magmatic fluids from the SJDD gabbro provide new lines of investigation regarding ore-forming processes and the potential of mafic magmas as a non-negligible metal sources. Indeed, late Devonian - early Carboniferous mafic magmatism is relatively widespread in the European Variscan belt (Pochon et al., 2016b; Villaseca et al., 2022) and spatially related to Sb ± Hg mineralisation (Arribas and Gumiel, 1984; Higueras et al. 2013; Pochon et al., 2016a, 2019).

5.4 Towards an alteration model for the SJDD gabbro

Our 3D geological modeling has confirmed that the SJDD intrusive complex has a sill-like shape and that the SJDD gabbro is much thicker in the eastern part than in the partially eroded western part. This geometry agrees with the fact that the western part corresponds to the lower part of the intrusion, whereas the eastern part corresponds to the intrusion roof. The three studied main zones along the E-W cross-section thus present distinct mineral assemblages that reflect an increasing alteration of the primary phases from west to east (textural and mineralogical observations summarized in Table 1). Calcic plagioclase is well-preserved in the lower part of the gabbro, whereas it is partially saussuritized in the central part and completely altered into albite, epidote and sericite in the intrusion roof. Similarly, clinopyroxene is commonly partially replaced by actinolite in the lower part, rare in the central part and absent (i.e. probably entirely replaced) in the intrusion roof. Moreover, ilmenite is fresh in the lower part, whereas it contains many fluid inclusions and is partially replaced by titanite and rutile in the central part and intrusion roof. The abundance of fluid inclusions increases toward the intrusion roof.

Volatiles appear to play a major role in the alteration and the cooling history of the SJDD gabbro, especially during the late magmatic stage with the crystallization of hydrous phases, and the entrapment of fluid inclusions in ilmenite. Moreover, magmatic fluids also seem to control the subsolidus alteration of the SJDD gabbro, including (i) saussuritization, (ii) replacement of clinopyroxene by actinolite and (iii) breakdown of ilmenite into titanite and rutile. Saussuritization indicates fluid-induced breakdown of plagioclase at elevated temperatures (Goldsmith, 1982), and is observed to occur in mafic pegmatites (Heckmann et al., 2022 and references therein). Amphibole-forming reactions reflect a continuous retrograde thermal evolution and record the cooling history of the pluton. The synthetic illustration given in Figure 11 summarizes how mineral assemblages evolve from magmatic-dominated in the lower part, to magmatic-hydrothermal in the central part and then to hydrothermal-dominated in the intrusion roof. This depicts a progressive alteration gradient increasing from the lower part to the intrusion roof, induced by pervasive infiltration of fluids that we propose to be mainly of magmatic origin. The involvement of external meteoric-derived fluids or felsic-derived magmatic fluids (e.g. felsic facies are concomitant with mafic facies) cannot be excluded. However, infiltration of such external fluid in

disequilibrium with mafic rocks would have affected the geochemistry of the gabbro to a higher extent, as it is the case for hydrothermally altered dolerites or the altered gabbros of the Chenaillet Ophiolite (Figs. 3b and c). The formers underwent obvious potassic alteration caused by meteoric fluids (Pochon et al., 2016), whereas the latters underwent sodic alteration probably caused by albititic hydrous melt (Tribuzio et al., 2019) or seawater (Nicollet et al., 2022). The SJDD gabbro does not seem to be concerned by these alterations.

As the SJDD pluton is likely to have formed by under-accretion of several mafic sills (Barboni et al., 2013), magmatic fluids may have derived from the exsolution of volatiles from underlying sills and consequently affected the overlying sills that were almost crystallized. Furthermore, the magmatic origin of the fluids is consistent with what is illustrated by the K_2O+Na_2O vs. $K_2O/(K_2O+Na_2O)$ diagram (Fig. 3b) and the CCPI vs. AI diagram (Fig. 3c). The alteration features of the upper part of the SJDD gabbros are similar to hornblende gabbros from Pe-Piper et al. (2010) which have undergone autometasomatic alteration. This also shows that most of the mobile elements (i.e. Si, Na, K) are not always strongly affected by magmatic fluids, which explains why mafic-derived magmatic fluids alter much less the original chemical features of mafic rocks than meteoric or felsic-derived magmatic fluids. However, as exsolved magmatic volatiles rise upwards, they necessarily modify the composition of overlying crystallized magmas at the mineral scale, mainly depending on the fluid/mineral ratio, the length scale of their circulation path and the mineral's reactivity to fluid chemistry. Plagioclase is one of the first phase to react as it is not in equilibrium with late stage magmatic fluids. The observed alteration of the SJDD could therefore be referred to as an autometasomatic process (i.e. deuteric alteration, Elsdon et al. 1982; Bartley et al., 2020). Fluids promoted the destabilization of clinopyroxene, brown pargasite and calcic plagioclase (i.e. saussuritization), which lead to a mineral assemblage composed of magnesio-hornblende, actinolite, albite, epidote and sericite. The release of SiO_2 and Ca allowed ilmenite breakdown into titanite. Then, rutile began to grow as a result of decreasing temperature accompanied by consumption of Ca by epidote, titanite and apatite. Such replacement processes reflect the magmatic-hydrothermal transition, which occurred as the pluton progressively cooled down.

6. Conclusions

By combining 3D geological modeling, whole-rock geochemistry, detailed mineralogical and textural observations, and major and trace element chemical analyses, a conceptual model is proposed to explain the alteration gradient observed in the SJDD intrusive complex. The most significant conclusions are as follows:

1. 3D geological modeling confirms the sill-like shape of the SJDD intrusive complex, and consequently indicates that the western part corresponds to the lower part of the intrusion, whereas the eastern part represents the intrusion roof.

2. Water played a major role in the evolution of the SJDD gabbro from the late magmatic to the high-temperature hydrothermal stage. The presence of magmatic hydrous minerals such as magnesio-hastingsite indicates significant presence of dissolved water at the magmatic stage, while

saussuritization and amphibole-forming reactions reflect fluid-induced alteration, a continuous retrograde thermal evolution during cooling.

3. Ilmenite has a peculiar texture in the SJDD intrusive complex. Whereas it is relatively fresh in the lower part, it entraps a high abundance of probably magmatic fluid inclusions inside its core in the central part and the intrusion roof.

4. Our study demonstrate that ilmenite may be an efficient trap for fluids and consequently an excellent but underestimated archivist of the magmatic-hydrothermal transition at least in mafic systems.

5. We document progressive hydrous alteration from the lower part to the roof of the intrusion highlighted by progressive fluid-driven mineral replacements, probably induced by the upward rise of exsolved magmatic fluids along grain boundaries of overlying crystallized sills.

6. Through our observations, we propose that most of the observed replacement reactions in the SJDD intrusive complex are the result of an autometasomatic alteration and we suggest that this process needs to be reassessed and better understood in mafic systems.

7. The relative enrichment of metals in mafic-derived magmatic fluids needs to be further considered and evaluated as it could indicate that the late Devonian – early Carboniferous mafic magmatism is a potential metal source in the European Variscan belt.

Acknowledgments

This work was carried out in the framework of the ERA-MIN2 Aureole project ("tArgeting eU cRitical mEtals (Sb, W) and predictibility of Sb-As-Hg envirOnmentaL issuEs") and funded by the ANR (grant ANR-19-MIN2-0002) for the French partners. The LabEx VOLTAIRE (ANR-10-LABX-100-01) and EquipEx PLANEX (ANR-11-EQPX-0036) are also acknowledged to have provided support to the electron microprobe and LA-ICP-MS laboratories. The authors thank Ida Di Carlo and Guillaume Wille for their help with the EPMA analyses, and Daniel Kontak for the useful discussions that greatly improved the final version of the paper. The reviewers are acknowledged for their constructive remarks.

References

Allard, P., Aiuppa, A., Loyer, H., Carrot, F., Gaudry, A., Pinte, G., Michel, A., Dongarrà, G., 2000. Acid gas and metal emission rates during long-lived basalt degassing at Stromboli volcano. Geophys. Res. Lett. 27, 1207–1210. https://doi.org/10.1029/1999GL008413.

Angiboust, S., Harlov, D., 2017. Ilmenite breakdown and rutile-titanite stability in metagranitoids: Natural observations and experimental results. Am. Mineral. 102, 1696–1708. https://doi.org/10.2138/am-2017-6064.

Arribas, A., Gumiel, P., 2011. First Occurrence of a Strata-Bound Sb-W-Hg Deposit in the Spanish Hercynian Massif, in: Syngenesis and Epigenesis in the Formation of Mineral Deposits. Springer Berlin Heidelberg, pp. 468–481. https://doi.org/10.1007/978-3-642-70074-3_43.

Ballèvre, M., Le Goff, E., Hébert, R., 2001. The tectonothermal evolution of the Cadomian belt of northern Brittany, France: a Neoproterozoic volcanic arc. Tectonophysics 331, 19–43. https://doi.org/10.1016/S0040-1951(00)00234-.

Ballèvre, M., Martínez Catalan, J.R., López-Carmona, A., Pitra, P., Abati, J., Fernández, R.D., Ducassou, C., Arenas, R., Bosse, V., Castiñeiras, P., Fernández-Suárez, J., Barreiro, J.G., Paquette, J.L., Peucat, J.J., Poujol, M., Ruffet, G., Martínez, S.S., 2014. Correlation of the nappe stack in the Ibero-Armorican arc across the Bay of Biscay: A joint French-Spanish project. Geol. Soc. Spec. Publ. 405, 77–113. https://doi.org/10.1144/SP405.13.

Barboni, M., Bussy, F., Chiaradia, M., 2011. Origin of Early Carboniferous pseudo-adakites in northern Brittany (France) through massive amphibole fractionation from hydrous basalt. Terra Nov. 23, 1–10. https://doi.org/10.1111/j.1365-3121.2010.00974.x.

Barboni, M., Schoene, B., Ovtcharova, M., Bussy, F., Schaltegger, U., Gerdes, A., 2013. Timing of incremental pluton construction and magmatic activity in a back-arc setting revealed by ID-TIMS U/Pb and Hf isotopes on complex zircon grains. Chem. Geol. 342, 76–93. https://doi.org/10.1016/j.chemgeo.2012.12.011.

Bartley, J.M., Glazner, A.F., Stearns, M.A., Coleman, D.S., 2020. The granite aqueduct and autometamorphism of plutons. Geosci. 10, 136. https://doi.org/10.3390/geosciences10040136.

Beckman, V., Möller, C., 2018. Prograde metamorphic zircon formation in gabbroic rocks: The tale of microtextures. J. Metamorph. Geol. 36, 1221–1236. https://doi.org/10.1111/jmg.12443.

Blundy, J., Cashman, K., 2008. Petrologic reconstruction of magmatic system variables and processes. Rev. Mineral. Geochemistry 69, 179–239. https://doi.org/10.2138/rmg.2008.69.6.

Bodnar, R.J., 2003. Reequilibration of fluid inclusions. In I. Samson, A. Anderson, & D. Marshall, eds. Fluid Inclusions: Analysis and Interpretation. Mineral. Assoc. Canada, Short Course 32, 213-230.

Brun, J.P., Guennoc, P., Truffert, C., Vairon, J., 2001. Cadomian tectonics in northern Brittany: A contribution of 3-D crustal-scale modelling. Tectonophysics 331, 229–246. https://doi.org/10.1016/S0040-1951(00)00244-4.

Calcagno, P., Chilès, J.P., Courrioux, G., Guillen, A., 2008. Geological modelling from field data and geological knowledge. Part I. Modelling method coupling 3D potential-field interpolation and geological rules. Phys. Earth Planet. Inter. 171, 147–157. https://doi.org/10.1016/j.pepi.2008.06.013.

Caroff, M., Coint, N., Hallot, E., Hamelin, C., Peucat, J.J., Charreteur, G., 2011. The mafic-silicic layered intrusions of Saint-Jean-du-Doigt (France) and North-Guernsey (Channel Islands), Armorican Massif: Gabbro-diorite layering and mafic cumulate-pegmatoid association. Lithos 125, 675–692. https://doi.org/10.1016/j.lithos.2011.03.019.

Chantraine J., Barrière M., Cabanis B., Chauris L., Herrouin Y., Rabu D., Weecksteen G., Chauris MM., Larsonneur C., Autran A. 1985. Carte géol. France (1/50 000), feuille Plestin-Les-Grèves (202). BRGM, Orléans.

Chantraine, J., Egal, E., Thiéblemont, D., Le Goff, E., Guerrot, C., Ballèvre, M., Guennoc, P., 2001. The Cadomian active margin (North Armorican Massif, France): A segment of the North Atlantic Panafrican belt. Tectonophysics 331, 1–18. https://doi.org/10.1016/S0040-1951(00)00233-X.

Coint, N., Hamelin, C., Caroff, M., 2008. Le complexe gabbro-dioritique lité de SaintJean-du-Doigt, Massif armoricain: un exemple de réservoir magmatique de type MASLI. Bulletin de la Société Géologique et Minéralogique de Bretagne (D) 5, 1–29.

Droop, G.T.R., 1987. A general equation for estimating Fe 3+ concentrations in ferromagnesian silicates and oxides from microprobe analyses, using stoichiometric criteria. Mineral. Mag. 51, 431–435. https://doi.org/10.1180/minmag.1987.051.361.10.

Egal, E., Guerrot, C., Le Goff, E., Thiéblemont, D., Chantraine, J., 1996. The Cadomian orogeny revisited in northern Brittany (France). In: Nance, E.D., Thompson, M.D. (Eds.), Avalonian and related peri-Gondwana terranes of the circum-north Atlantic. Geol. Soc. Am. Spec. Pap., 304, 281-318.

Elsdon, R., 1982. Autometasomatic alteration of gabbro, Kap Edvard Holm intrusive complex, East Greenland. Mineral. Mag. 45, 219-225.

France, L., Koepke, J., Ildefonse, B., Cichy, S.B., Deschamps, F., 2010. Hydrous partial melting in the sheeted dike complex at fast spreading ridges: Experimental and natural observations. Contrib. to Mineral. Petrol. 160, 683–704. https://doi.org/10.1007/s00410-010-0502-0.

Fulignati, P., Kamenetsky, V.S., Marianelli, P., Sbrana, A., Meffre, S., 2011. First insights on the metallogenic signature of magmatic fluids exsolved from the active magma chamber of Vesuvius (AD 79 “Pompei” eruption). J. Volcanol. Geotherm. Res. 200, 223–233. https://doi.org/10.1016/j.jvolgeores.2010.12.015.

Gifkins, C., Herrmann, W., Large, R., 2005. Altered Volcanic Rocks: A Guide to Description and Interpretation. Centre for Ore Deposit Research, University of Tasmania, Hobart, 288 p.

Gonnermann, H.M., Manga, M., 2007. The fluid mechanics inside a volcano. Annu. Rev. Fluid Mech. https://doi.org/10.1146/annurev.fluid.39.050905.110207.

Grove, T.L., Elkins-Tanton, L.T., Parman, S.W., Chatterjee, N., Müntener, O., Gaetani, G.A., 2003. Fractional crystallization and mantle-melting controls on calc-alkaline differentiation trends. Contrib. to Mineral. Petrol. 145, 515–533. http://doi.org/10.1007/s00410-003-0448-z

Goldsmith, J.R., 1982. Plagioclase stability at elevated temperatures and water pressures. Am. Mineral. 67, 653–675.

Hawthorne, F.C., Oberti, R., Harlow, G.E., Maresch, W. V., Martin, R.F., Schumacher, J.C., Welch, M.D., 2012. Ima report: Nomenclature of the amphibole supergroup. Am. Mineral. 97, 2031–2048. https://doi.org/10.2138/am.2012.4276.

Hayden, L.A., Watson, E.B., Wark, D.A., 2008. A thermobarometer for sphene (titanite). Contrib. to Mineral. Petrol. 155, 529–540. https://doi.org/10.1007/s00410-007-0256-y.

Heckmann, P., Palinkaš, S.S., Hansen, H., Iacono-Marziano, G., Rajič, K., Forien, M., Bergh, S.G., 2022. Petrogenesis of zoned and unzoned mafic pegmatites: An insight from the Palaeoproterozoic mafic-ultramafic Hamn intrusion, Northern Norway. Lithos 428–429, 106818. https://doi.org/10.1016/j.lithos.2022.106818.

Hedenquist, J.W., Lowenstern, J.B., 1994. The role of magmas in the formation of hydrothermal ore deposits. Nature. https://doi.org/10.1038/370519a0.

Henley, R.W., Berger, B.R., 2013. Nature's refineries - Metals and metalloids in arc volcanoes. Earth-Science Rev. https://doi.org/10.1016/j.earscirev.2013.07.007.

Higueras, P., Oyarzun, R., Lillo, J., Morata, D., 2013. Intraplate mafic magmatism, degasification, and deposition of mercury: The giant Almadén mercury deposit (Spain) revisited. Ore Geol. Rev. 51, 93–102. https://doi.org/10.1016/j.oregeorev.2012.12.004.

Holland, T., Blundy, J., 1994. Non-ideal interactions in calcic amphiboles and their bearing on amphibole-plagioclase thermometry. Contrib. to Mineral. Petrol. 116, 433–447. https://doi.org/10.1007/BF00310910.

Hughes, C.J., 1973. Spilites, keratophyres and the igneous spectrum. Geol. Mag. 503–527.

Jamieson, J.C., Olinger, B., 1969. Pressure-temperature studies of anatase, brookite rutile, and TiO_2 (II): A discussion. Am. Mineral. 54, 1477–1481.

Janssen, A., Putnis, A., Geisler, T., Putnis, C. V., 2010. The experimental replacement of ilmenite by rutile in HCl solutions. Mineral. Mag. 74, 633–644. https://doi.org/10.1180/minmag.2010.074.4.633.

Klemme, S., Günther, D., Hametner, K., Prowatke, S., Zack, T., 2006. The partitioning of trace elements between ilmenite, ulvospinel, armalcolite and silicate melts with implications for the early differentiation of the moon. Chem. Geol. 234, 251–263. https://doi.org/10.1016/j.chemgeo.2006.05.005.

Kohn, M.J., 2020. A refined zirconium-in-rutile thermometer. Am. Mineral. 105, 963–971. https://doi.org/10.2138/am-2020-7091.

Lajaunie, C., Courrioux, G., Manuel, L., 1997. Foliation fields and 3D cartography in geology: Principles of a method based on potential interpolation. Math. Geol. 29, 571–584. https://doi.org/10.1007/bf02775087.

Large, R.R., Gemmell, J.B., Paulick, H., 2001. The alteration box plot: A simple approach to understanding the relationship between alteration mineralogy and lithogeochemistry associated with volcanic-hosted massive sulfide deposits. Econ. Geol. 96, 957–971. https://doi.org/10.2113/gsecongeo.96.5.957.

Lewis, M.J., Bucholz, C.E., Jagoutz, O.E., 2021. Evidence for polybaric fractional crystallization in a continental arc: Hidden Lakes mafic complex, Sierra Nevada batholith, California. Contrib. to Mineral. Petrol. 176, 1–27. https://doi.org/10.1007/s00410-021-01844-y.

Liao, Y., Wei, C., Rehman, H.U., 2021. Titanium in calcium amphibole: Behavior and thermometry. Am. Mineral. 106, 180–191. https://doi.org/10.2138/am-2020-7409.

Liou, J.G., Zhang, R., Ernst, W.G., Liu, J., McLimans, R., 1998. Mineral parageneses in the Piampaludo eclogitic body, Gruppo di Voltri, western Ligurian Alps. Schweizerische Mineral. und Petrogr. Mitteilungen 78, 317–335.

Martínez Catalán, J.R., Schulmann, K., Ghienne, J.F., 2021. The Mid-Variscan Allochthon: Keys from correlation, partial retrodeformation and plate-tectonic reconstruction to unlock the geometry of a non-cylindrical belt. Earth-Science Rev. https://doi.org/10.1016/j.earscirev.2021.103700.

Matte, P., 1986. Tectonics and plate tectonics model for the Variscan belt of Europe. Tectonophysics 126, 329–374. https://doi.org/10.1016/0040-1951(86)90237-4.

McDonough, W.F., Sun, S.S., 1995. The composition of the Earth. Chem. Geol., Chemical {Evolution} of the {Mantle} 120, 223–253. https://doi.org/10.1016/0009-2541(94)00140-4.

Mullan, H.S., Bussell M.A., 1977. The basic rock series in batholithic associations. Geol. Mag. 114, 265–280. https://doi.org/10.1017/S0016756800045064.

Nicollet, C., Paquette, J.-L., Bruand, E., Bosse, V., Pereira, I., 2022. Crystallisation and fast cooling of the (meta)gabbro from the Chenaillet ophiolite (Western Alps): In-situ U Pb dating of zircon, titanite, monazite and xenotime in textural context. Lithos 414–415, 106620. https://doi.org/10.1016/j.lithos.2022.106620.

Otten, M.T., 1984. The origin of brown hornblende in the Artfjället gabbro and dolerites. Contrib. to Mineral. Petrol. 86, 189–199. https://doi.org/10.1007/BF00381846.

Paton, C., Hellstrom, J., Paul, B., Woodhead, J., Hergt, J., 2011. Iolite: Freeware for the visualisation and processing of mass spectrometric data. J. Anal. At. Spectrom. 26, 2508–2518. https://doi.org/10.1039/c1ja10172b.

Pearce, M., Escolme, A., 2021. Phase heritage during replacement reactions in Ti-bearing minerals. Contrib. to Mineral. Petrol. 176, 1–18. https://doi.org/10.1007/s00410-021-01775-8.

Pe-Piper, G., Piper, D.J.W., Tsikouras, B., 2010. The late neoproterozoic frog lake hornblende gabbro pluton, Avalon Terrane of Nova Scotia: Evidence for the origins of appinites. Can. J. Earth Sci. 47, 103–120. https://doi.org/10.1139/E09-077.

Pertsev, A.N., Aranovich, L.Y., Prokofiev, V.Y., Bortnikov, N.S., Cipriani, A., Simakin, S.S., Borisovskiy, S.E., 2015. Signatures of residual melts, magmatic and seawater-derived fluids in oceanic lower-crust gabbro from the vema lithospheric section, central Atlantic. J. Petrol. 56, 1069–1088. https://doi.org/10.1093/petrology/egv028.

Pochon, A., 2017. Magmatisme mafique et minéralisations Sb-Au dans le domaine Centre Armoricain: contrôles spatio-temporels et implications metallogéniques (Doctoral dissertation, Université Rennes 1), 312 p.

Pochon, A., Beaudoin, G., Branquet, Y., Boulvais, P., Gloaguen, E., Gapais, D., 2017. Metal mobility during hydrothermal breakdown of Fe-Ti oxides: Insights from Sb-Au mineralizing event (Variscan Armorican Massif, France). Ore Geol. Rev. 91, 66–99. https://doi.org/10.1016/J.OREGEOREV.2017.10.021.

Pochon, A., Branquet, Y., Gloaguen, E., Ruffet, G., Poujol, M., Boulvais, P., Gumiaux, C., Cagnard, F., Baele, J.M., Kéré, I., Gapais, D., 2019. A Sb ± Au mineralizing peak at 360 Ma in the Variscan belt. BSGF - Earth Sci. Bull. 190. https://doi.org/10.1051/bsgf/2019004.

Pochon, A., Gapais, D., Gloaguen, E., Gumiaux, C., Branquet, Y., Cagnard, F., Martelet, G., 2016a. Antimony deposits in the Variscan Armorican belt, a link with mafic intrusives? Terra Nov. 28, 138–145. https://doi.org/10.1111/ter.12201.

Pochon, A., Gloaguen, E., Branquet, Y., Poujol, M., Ruffet, G., Boiron, M.C., Boulvais, P., Gumiaux, C., Cagnard, F., Gouazou, F., Gapais, D., 2018. Variscan Sb-Au mineralization in Central Brittany (France): A new metallogenic model derived from the Le Semnon district. Ore Geol. Rev. 97, 109–142. https://doi.org/10.1016/j.oregeorev.2018.04.016.

Pochon, A., Poujol, M., Gloaguen, E., Branquet, Y., Cagnard, F., Gumiaux, C., Gapais, D., 2016b. U-Pb LA-ICP-MS dating of apatite in mafic rocks: Evidence for a major magmatic event at the Devonian-Carboniferous boundary in the Armorican Massif (France). Am. Mineral. 101, 2430–2442. https://doi.org/10.2138/am-2016-5736.

Putirka, K., 2016. Amphibole thermometers and barometers for igneous systems and some implications for eruption mechanisms of felsic magmas at arc volcanoes. Am. Mineral. 101, 841–858. https://doi.org/10.2138/am-2016-5506.

Putnis, A., 2009. 3. Mineral Replacement Reactions, in: Thermodynamics and Kinetics of Water-Rock Interaction. De Gruyter, pp. 87–124. https://doi.org/10.1515/9781501508462-005.

Putnis, A., Austrheim, H., 2010. Fluid-induced processes: Metasomatism and metamorphism. Geofluids 10, 254–269. https://doi.org/10.1111/j.1468-8123.2010.00285.x.

Raase, P., 1974. Al and Ti contents of hornblende, indicators of pressure and temperature of regional metamorphism. Contrib. to Mineral. Petrol. 45, 231–236. https://doi.org/10.1007/BF00383440.

Ridolfi, F., Renzulli, A., 2012. Calcic amphiboles in calc-alkaline and alkaline magmas: Thermobarometric and chemometric empirical equations valid up to 1,130°C and 2.2 GPa. Contrib. to Mineral. Petrol. 163, 877–895. https://doi.org/10.1007/s00410-011-0704-6.

Ridolfi, F., Renzulli, A., Puerini, M., 2010. Stability and chemical equilibrium of amphibole in calc-alkaline magmas: An overview, new thermobarometric formulations and application to subduction-related volcanoes. Contrib. to Mineral. Petrol. 160, 45–66. https://doi.org/10.1007/s00410-009-0465-7.

Ridolfi, F., Zanetti, A., Renzulli, A., Perugini, Di., Holtz, F., Oberti, R., 2018. AMFORM, a new mass-based model for the calculation of the unit formula of amphiboles from electron microprobe analyses. Am. Mineral. 103, 1112–1125. https://doi.org/10.2138/am-2018-6385.

Santos, C.A., White, R.W., Moraes, R., Szabó, G.A.J., 2021. The gabbro to amphibolite transition along a hydration front. J. Metamorph. Geol. 39, 417–442. https://doi.org/10.1111/jmg.12582.

Sun, S., McDonough, W.F., 1989. Chemical and isotopic systematics of oceanic basalts: implications for mantle composition and processes. Geol. Soc. London, Spec. Publ. 42, 313–345. https://doi.org/10.1144/GSL.SP.1989.042.01.19.

Tomkins, H.S., Powell, R., Ellis, D.J., 2007. The pressure dependence of the zirconium-in-rutile thermometer. J. Metamorph. Geol. 25, 703–713. https://doi.org/10.1111/j.1525-1314.2007.00724.x.

Tribuzio, R., Manatschal, G., Renna, M.R., Ottolini, L., Zanetti, A., 2020. Tectono-magmatic interplay and related metasomatism in gabbros of the chenaillet ophiolite (western alps). J. Petrol. 60, 2483–2508. https://doi.org/10.1093/petrology/egaa015.

Vigneresse, J.L., Truche, L., Richard, A., 2019. How do metals escape from magmas to form porphyry-type ore deposits? Ore Geol. Rev. 105, 310–336. https://doi.org/10.1016/j.oregeorev.2018.12.016.

Villaseca, C., Orejana, D., Higueras, P., Pérez-Soba, C., García Serrano, J., Lorenzo, S., 2022. The evolution of the subcontinental mantle beneath the Central Iberian Zone: Geochemical tracking of its mafic magmatism from the Neoproterozoic to the Cenozoic. Earth-Science Rev. https://doi.org/10.1016/j.earscirev.2022.103997.

Wechsler, B.A., Prewitt, C.T., 1984. Crystal structure of ilmenite (FeTiO3) at high temperature and at high pressure. Am. Mineral. 69, 176–185.

Williams-Jones, A.E., Heinrich, C.A., 2005. Vapor transport of metals and the formation of magmatic-hydrothermal ore deposits. Econ. Geol. 100, 1287–1312. https://doi.org/10.2113/gsecongeo.100.7.1287.

Zack, T., von Eynatten, H., Kronz, A., 2004. Rutile geochemistry and its potential use in quantitative provenance studies. Sediment. Geol., Quantitative Provenance Analysis of Sediments 171, 37–58. https://doi.org/10.1016/j.sedgeo.2004.05.009.

Zajacz, Z., Halter, W.E., Pettke, T., Guillong, M., 2008. Determination of fluid/melt partition coefficients by LA-ICPMS analysis of co-existing fluid and silicate melt inclusions: Controls on element partitioning. Geochim. Cosmochim. Acta 72, 2169–2197. https://doi.org/10.1016/j.gca.2008.01.034.

Zimmer, M.M., Plank, T., Hauri, E.H., Yogodzinski, G.M., Stelling, P., Larsen, J., Singer, B., Jicha, B., Mandeville, C., Nye, C.J., 2010. The role of water in generating the calc-alkaline trend: New volatile data for aleutian magmas and a new tholeiitic index. J. Petrol. 51, 2411–2444. https://doi.org/10.1093/petrology/egq062.

Figure 1. (a) Location of the studied area in the geodynamic framework of the Variscan Armorican belt (adapted from Ballèvre et al., 2014). The black rectangle indicates the location of Figure 1b. (b) Geological map of the eastern part of the NAD with the delimitation of the Pan-African litho-structural units. (c) Geological map of the SJDD intrusive complex (adapted from Chantraine et al., 1985). The three main zones of the gabbro were defined from the gravity data and 3D geological modeling. White dashed lines correspond to the interpreted delimitation between the three zones.

Figure 2. 3D views of the SJDD gabbro intrusion showing a general sill-like geometry. Studied localities and samples are located in the 3D geological model.

Figure 3. (a) Chemical classification based on the total alkali versus silica (TAS) diagram and boxplot. (b) Whole-rock compositions in the chemical diagram of Hughes (1973). (c) Box-plot diagram (modified from Large et al., 2001) showing the geochemical signatures of samples from the SJDD. Fields representing the least altered volcanic rocks (< 52 wt%, 52-63 wt%, 63-69 wt% and > 69 wt% SiO_2) are from Gifkins et al. (2005). (d) Chondrite-normalized REE distribution patterns for SJDD samples. The CI chondrite composition is from McDonough and Sun (1995) and the compositions of normal and enriched mid-ocean ridge basalts (N- and E-MORB) are from Sun and McDonough (1989). Data of hydrothermally altered dolerites (Pochon, 2017), amphibolitized hornblende gabbros (Pe-Piper et al., 2010) and altered gabbros of the Chevaillet Ophiolite (Tribuzio et al., 2019), are also shown. Squares represent samples from this study. Circles and shaded grey zone represent data from existing literature on the three parts of SJDD gabbro (Coint et al. 2008; Caroff et al. 2011 and Barboni et al. 2013).

Figure 4. Selected thin section micro-photographs illustrating the typical textures of the SJDD gabbro from the three main zones: the western part (a-c), the central part (d-f) and the eastern part (g-i). (a) Plagioclase laths (white dashed lines) are corroded by clinopyroxene-actinolite-dark green pargasite assemblage. (b) Preserved clinopyroxene and fresh calcic plagioclase (labradorite) are in direct contact without alteration phases. Note the fluid inclusions bands in actinolite along the former clinopyroxene cleavage plans (yellow arrow). (c) Dark green pargasite encloses former clinopyroxene replaced by actinolite. (d) Partially saussuritized plagioclase in the central part of SJDD pluton, accompanied by biotite and amphibole. (e) Large crystals of magnesio-hornblende enclosing plagioclase. Note the presence of both preserved and saussuritized plagioclase. (f) Replacement of a large clinopyroxene crystal by actinolite promoted by fractures (see yellow arrow). (g-h) Typical mineral assemblage of the eastern part composed of actinolite, saussuritized plagioclase, epidote and quartz. (i) Typical amphibole crystal with a core of brown pargasite and a rim of magnesio-hornblende, subsequently destabilized into actinolite (white dashed line). Abbreviations: Act – actinolite, Ap – apatite, Br. Mg-hst – brown magnesio-hastingsite, Bt – biotite, Cpy – chalcopyrite, Cpx – clinopyroxene, Gr. Prg – dark green pargasite, Ilm – ilmenite, Mg-hb – magnesio-hornblende, Pl – plagioclase, Po – pyrrhotite, ss. Pl – saussuritized plagioclase. PPL – plane polarized light and XPL – crossed polarized light.

Figure 5. Al_{tot} vs Ti apfu and Al_{tot} apfu vs Mg# variations of amphibole from the western (a-b), central (c-d) and eastern parts (e-f).

Figure 6. Chondrite-normalized REE distribution (a-c) and primitive mantle-normalized trace elements patterns (d-f) of each type of amphibole from the western, central and eastern part. Compositions of CI chondrite and primitive mantle are from McDonough and Sun (1995).

Figure 7. Selected BSE images illustrating the typical textures of ilmenite from the three main zones of the SJDD gabbro. (a) Typical ilmenite crystal from the western part (lower part of the intrusion), exsolution and inclusion-free. (b) Ilmenite crystal from the central part of the intrusion, hosting numerous fluid inclusions (FIs). (c) Typical ilmenite texture in the eastern (upper) part of the intrusion. The core of crystal is extremely rich in uniformly oriented FIs, whereas the crystal rim is FI-poor and irregularly surrounded by titanite. (d) FI-rich and FI-poor areas within an ilmenite crystal. (e) Detail of Fig. 7b, showing the negative crystals shape of FIs. The c-axis is perpendicular to the observed plane. (f) Detail of Fig. 7c, illustrating small aligned FIs. (g) Titanite and rutile replacing ilmenite: titanite is the dominant Ti phase, rutile forms crystals with more or less uniform crystallographic orientation subparallel to FIs alignment (shown by the yellow dashed line). (h) Detail of ilmenite replacement by titanite and rutile: rutile seems to postdate a crack that promoted the breakdown of ilmenite into titanite (see yellow arrow). Note the zircon at the grain boundary. (i) Nm-sized inclusions of baddeleyite in ilmenite crystals indicated by yellow arrows.

Figure 8. Compositional variations of ilmenite in SJDD mafic facies: (a) Fe2+ + Mn2+ vs Ti apfu and (b) Fe3+ vs Fe2+ + Mn2+ apfu. Box plots of trace element contents in ilmenite from LA-ICP-MS data, sorted by abundance of fluid inclusions (a) and location within the intrusion (b).

Figure 9. (a) BSE image of an ilmenite crystal from the eastern part of the intrusion. X-ray elemental maps of Ca (b), Fe (c), Ti (d), Si (e), and Al (f).

Figure 10. Calculated crystallization temperatures (T°C) of different minerals. The white diamonds indicate the average values and n indicates the number of considered crystals for each thermometer. See text for further explanation.

Figure 11. (a) Conceptual model of the alteration gradient of the SJDD intrusive complex. (b-d) Mineral assemblages induced by the retrograde thermal evolution of the gabbro.

Declaration of interests

☒The authors declare that they have no known competing financial interests or personal relationships that could have appeared to influence the work reported in this paper.

☐The authors declare the following financial interests/personal relationships which may be considered as potential competing interests:

Table 1

Table 1

Mineralogical description of samples from the three main zones of the SJDD gabbro

	Western part *Primel cove*	**Central part** *SJDD seashore*	**Eastern part** *Poul Rodou*
Paragenesis	Pl (40 vol%), Amph (40 vol%), Cpx (15 vol%), Ilm+Ap+Sulf+Zrn+Qz (5 vol%)	Pl (40 vol%), Amph (50 vol%), Bt (5 vol%) Ilm+Ap+Sulf+Zrn+Qz (5 vol%)	Pl (45 vol%), Amph (45 vol%), Ep+Bt+Chl+Orth (5 vol%) Ilm+Ap+Sulf+Zrn+Qz (5 vol%)
Plagioclase	An40-60, with no or minor saussuritization	An10-45, with partial saussuritization	An0-5, with strong saussuritization Rare K-feldspar
Clinopyroxene	Frequent, partially replaced by Act	Rare, mainly within pegmatoids facies	No observed
Amphibole	Act Green prg Mg-hbl Brown prg	Act Mg-hbl Brown prg Green prg	Act Mg-hbl Brown prg
Ilmenite	Without fluid inclusions	Frequent, with fluid inclusions and Ttn rim	Frequent, with fluid inclusions and Ttn and Rt rims

Abbreviations: Act – actinote, Amph – amphibole, An – anorthite, Ap – apatite, Bt – biotite, Chl – chlorite, Cpx – clinopyroxene, Ep – epidote, Orth – orthoclase, Ilm – ilmenite, (Mg)-Hbl – (magnesio)-hornblende, Pl – plagioclase, Prg – pargasite, Qz – quartz, Rt – rutile, Sulf – sulfides, Ttn – titanite, Zrn – zircon.

Highlights

- A progressive hydrous alteration is recorded from the intrusion base up to the roof
- Fluid-induced reactions are driven as exsolved magmatic volatiles rise upwards
- The observed replacement reactions document an autometasomatic alteration
- Ilmenite may be an excellent archivist of the magmatic-hydrothermal transition

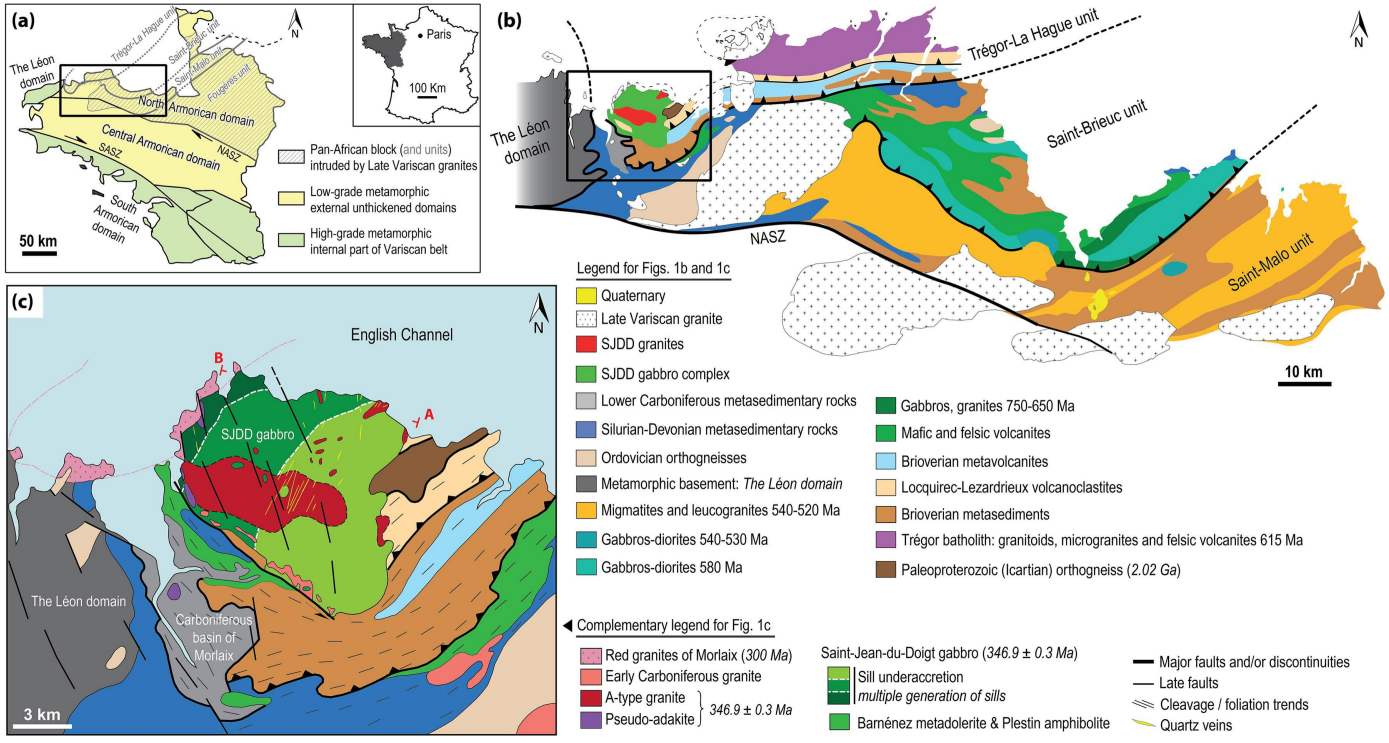
(a)
Trégor-La Hague unit
Saint-Brieuc unit
Saint-Malo unit
Fougères unit
The Léon domain
North Armorican domain
Central Armorican domain
South Armorican domain
NASZ
SASZ
N
Paris
100 Km
50 km
Pan-African block (and units) intruded by Late Variscan granites
Low-grade metamorphic external unthickened domains
High-grade metamorphic internal part of Variscan belt
(b)
Trégor-La Hague unit
Saint-Brieuc unit
Saint-Malo unit
The Léon domain
NASZ
N
10 km
Legend for Figs. 1b and 1c
Quaternary
Late Variscan granite
SJDD granites
SJDD gabbro complex
Lower Carboniferous metasedimentary rocks
Silurian-Devonian metasedimentary rocks
Ordovician orthogneisses
Metamorphic basement: The Léon domain
Migmatites and leucogranites 540-520 Ma
Gabbros-diorites 540-530 Ma
Gabbros-diorites 580 Ma
Gabbros, granites 750-650 Ma
Mafic and felsic volcanites
Brioverian metavolcanites
Locquirec-Lezardrieux volcanoclastites
Brioverian metasediments
Trégor batholith: granitoids, microgranites and felsic volcanites 615 Ma
Paleoproterozoic (Icartian) orthogneiss (2.02 Ga)
(c)
English Channel
N
B
A
SJDD gabbro
The Léon domain
Carboniferous basin of Morlaix
3 km
◀ Complementary legend for Fig. 1c
Red granites of Morlaix (300 Ma)
Early Carboniferous granite
A-type granite
Pseudo-adakite
346.9 ± 0.3 Ma
Saint-Jean-du-Doigt gabbro (346.9 ± 0.3 Ma)
Sill underaccretion
multiple generation of sills
Barnénez metadolerite & Plestin amphibolite
Major faults and/or discontinuities
Late faults
Cleavage / foliation trends
Quartz veins

Figure 1

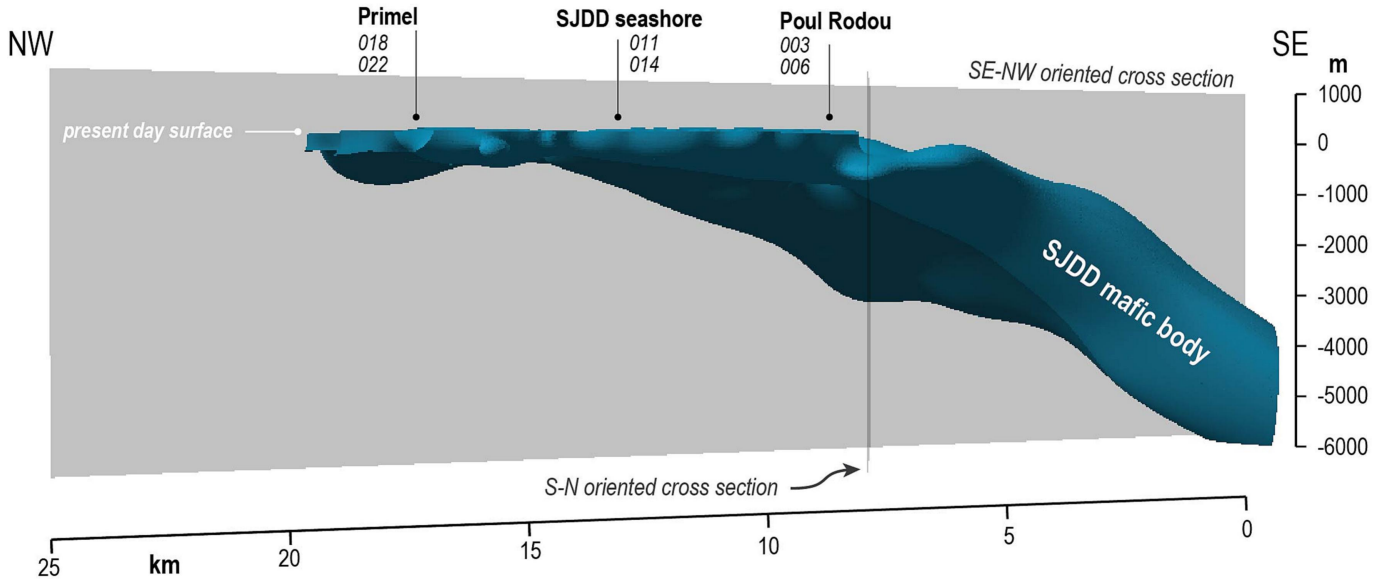
NW
SE
Primel
018
022
SJDD seashore
011
014
Poul Rodou
003
006
SE-NW oriented cross section
present day surface
SJDD mafic body
m
1000
0
-1000
-2000
-3000
-4000
-5000
-6000
S-N oriented cross section
25
km
20
15
10
5
0

Figure 2

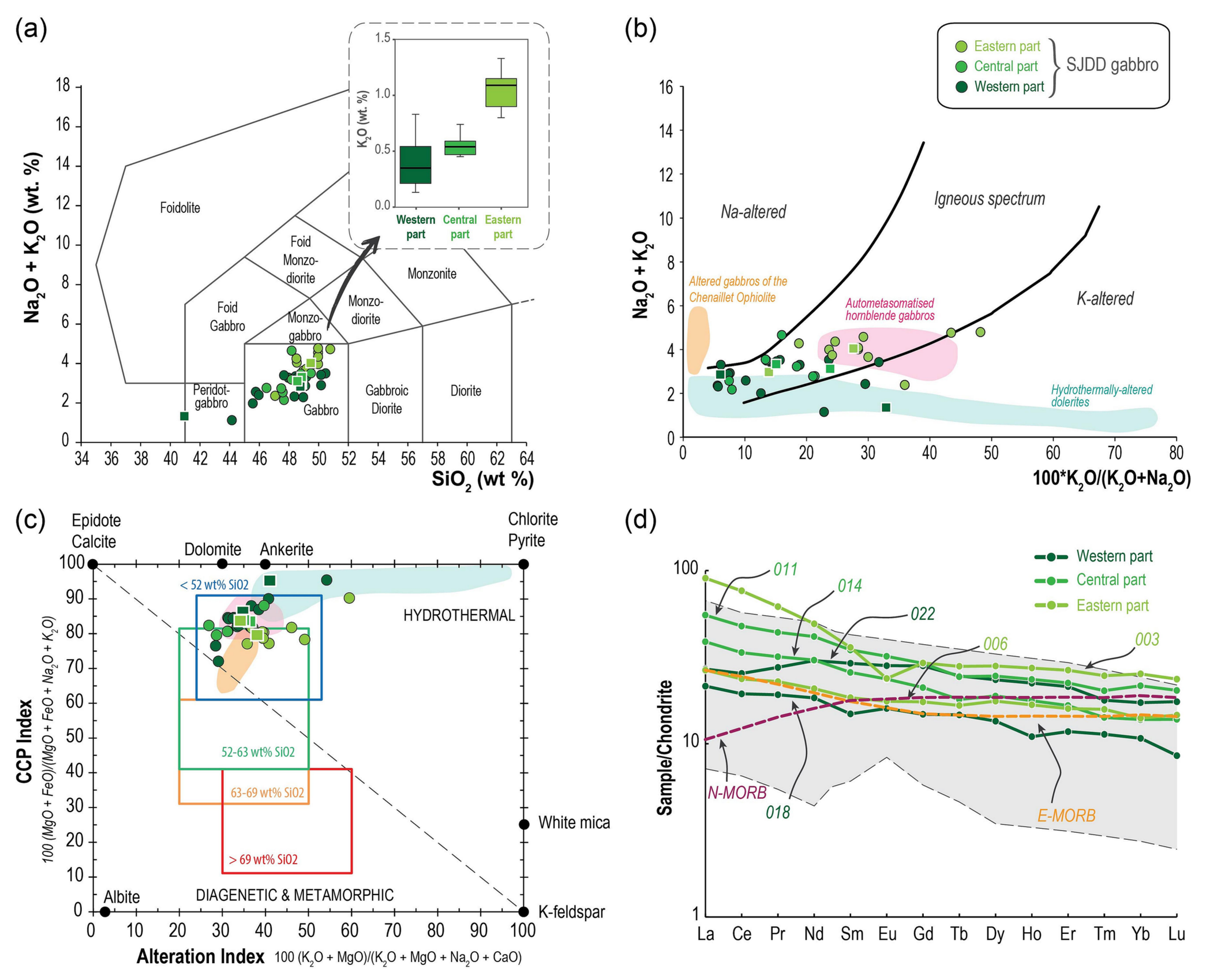
(a)
Foidolite
Foid Monzo-diorite
Monzonite
Foid Gabbro
Monzo-gabbro
Monzo-diorite
Peridot-gabbro
Gabbro
Gabbroic Diorite
Diorite
Na2O + K2O (wt. %)
SiO2 (wt %)
K2O (wt. %)
Western part
Central part
Eastern part
(b)
Eastern part
Central part
Western part
SJDD gabbro
Na-altered
Igneous spectrum
K-altered
Altered gabbros of the Chenaillet Ophiolite
Autometasomatised hornblende gabbros
Hydrothermally-altered dolerites
Na2O + K2O
100*K2O/(K2O+Na2O)
(c)
Epidote
Calcite
Dolomite
Ankerite
Chlorite
Pyrite
< 52 wt% SiO2
HYDROTHERMAL
52-63 wt% SiO2
63-69 wt% SiO2
> 69 wt% SiO2
White mica
Albite
DIAGENETIC & METAMORPHIC
K-feldspar
CCP Index
100 (MgO + FeO)/(MgO + FeO + Na2O + K2O)
Alteration Index
100 (K2O + MgO)/(K2O + MgO + Na2O + CaO)
(d)
Western part
Central part
Eastern part
011
014
022
006
003
018
N-MORB
E-MORB
Sample/Chondrite
La
Ce
Pr
Nd
Sm
Eu
Gd
Tb
Dy
Ho
Er
Tm
Yb
Lu

Figure 3

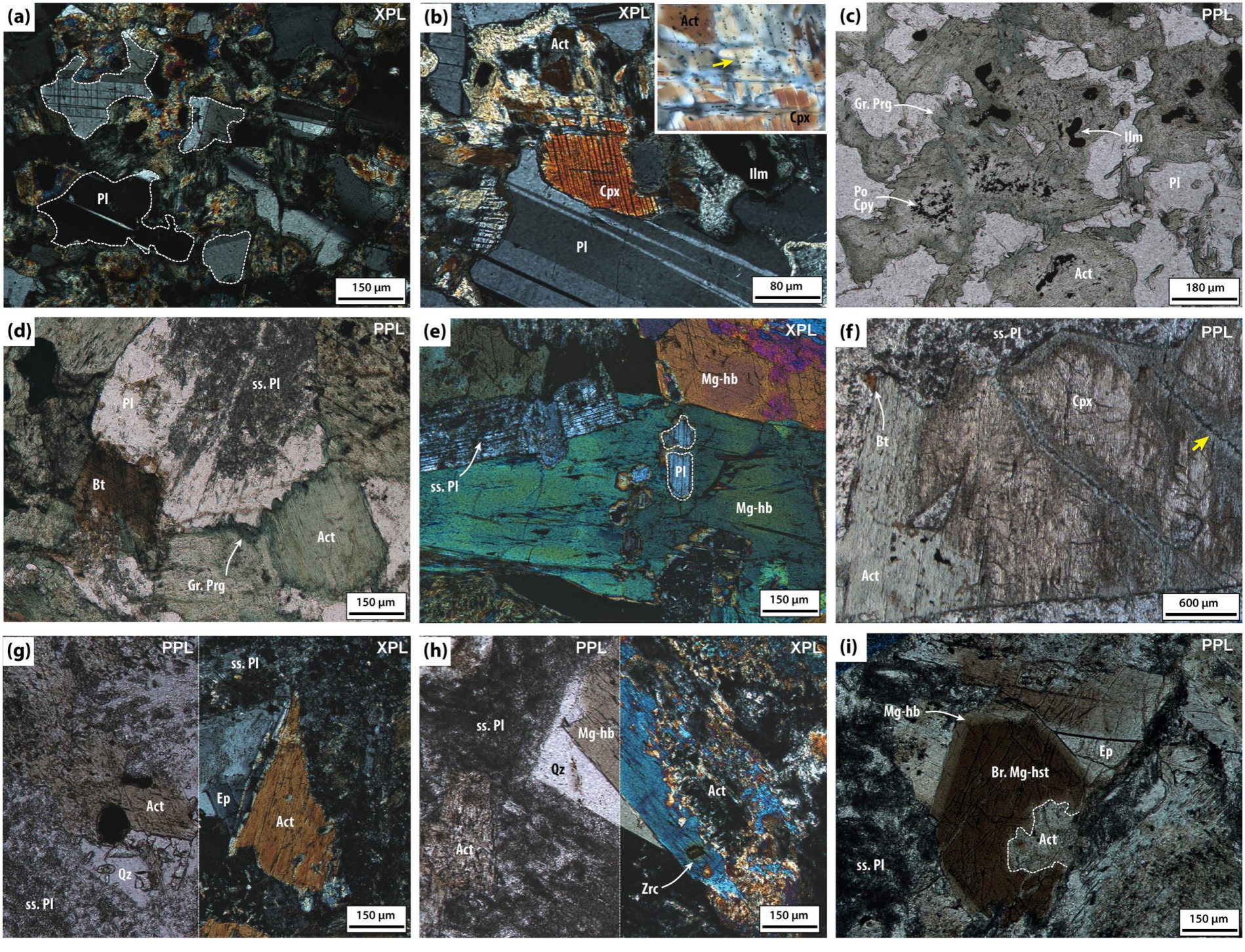
(a)
XPL
Pl
150 µm
(b)
XPL
Act
Cpx
Ilm
Pl
80 µm
Act
Cpx
(c)
PPL
Gr. Prg
Ilm
Pl
Po
Cpy
Act
180 µm
(d)
PPL
Pl
ss. Pl
Bt
Act
Gr. Prg
150 µm
(e)
XPL
Mg-hb
ss. Pl
Pl
Mg-hb
150 µm
(f)
ss. Pl
PPL
Cpx
Bt
Act
600 µm
(g)
PPL
Act
Qz
ss. Pl
XPL
ss. Pl
Ep
Act
150 µm
(h)
PPL
ss. Pl
Mg-hb
Qz
Act
XPL
Act
Zrc
150 µm
(i)
PPL
Mg-hb
Ep
Br. Mg-hst
Act
ss. Pl
150 µm

Figure 4

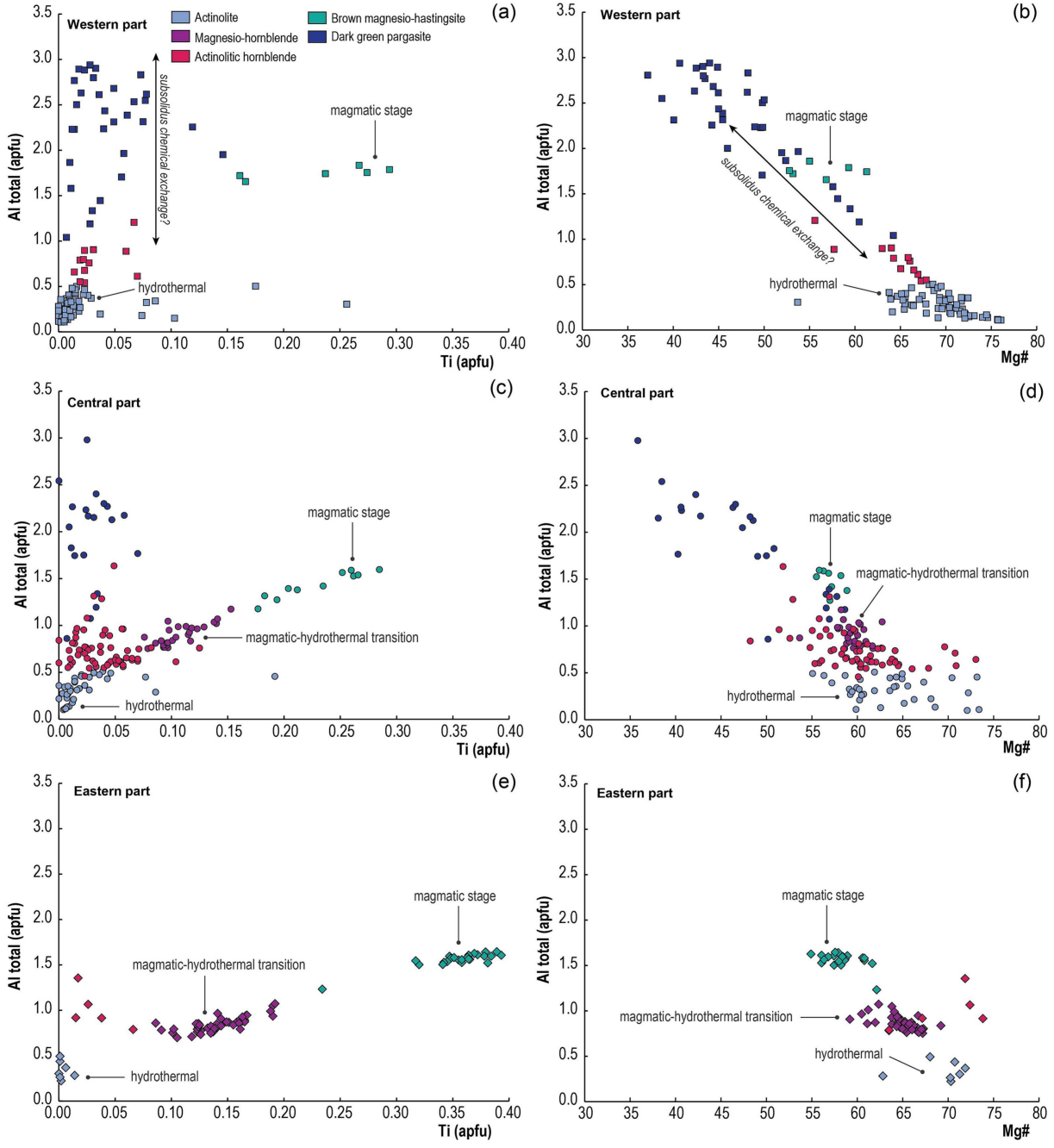
(a)
Western part
Actinolite
Magnesio-hornblende
Actinolitic hornblende
Brown magnesio-hastingsite
Dark green pargasite
subsolidus chemical exchange?
magmatic stage
hydrothermal
Al total (apfu)
Ti (apfu)
(b)
Western part
magmatic stage
subsolidus chemical exchange?
hydrothermal
Al total (apfu)
Mg#
(c)
Central part
magmatic stage
magmatic-hydrothermal transition
hydrothermal
Al total (apfu)
Ti (apfu)
(d)
Central part
magmatic stage
magmatic-hydrothermal transition
hydrothermal
Al total (apfu)
Mg#
(e)
Eastern part
magmatic stage
magmatic-hydrothermal transition
hydrothermal
Al total (apfu)
Ti (apfu)
(f)
Eastern part
magmatic stage
magmatic-hydrothermal transition
hydrothermal
Al total (apfu)
Mg#

Figure 5

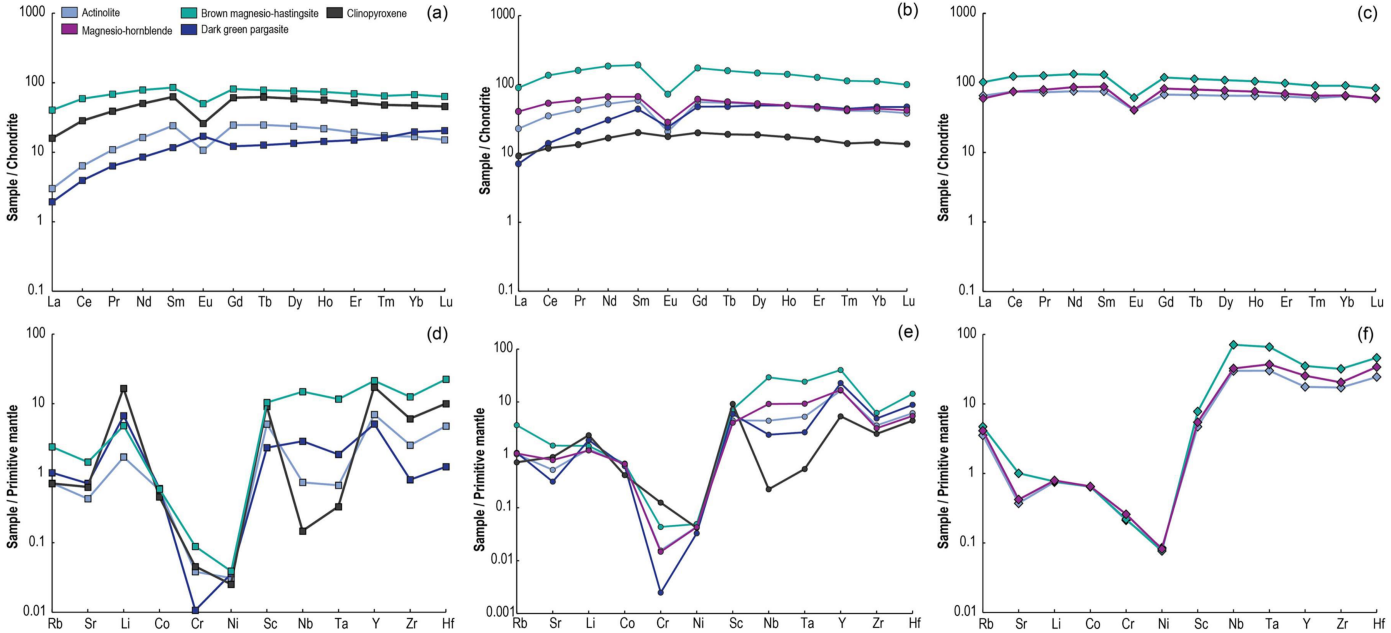
Actinolite
Magnesio-hornblende
Brown magnesio-hastingsite
Dark green pargasite
Clinopyroxene
(a)
(b)
(c)
(d)
(e)
(f)
Sample / Chondrite
Sample / Primitive mantle
La Ce Pr Nd Sm Eu Gd Tb Dy Ho Er Tm Yb Lu
Rb Sr Li Co Cr Ni Sc Nb Ta Y Zr Hf

Figure 6

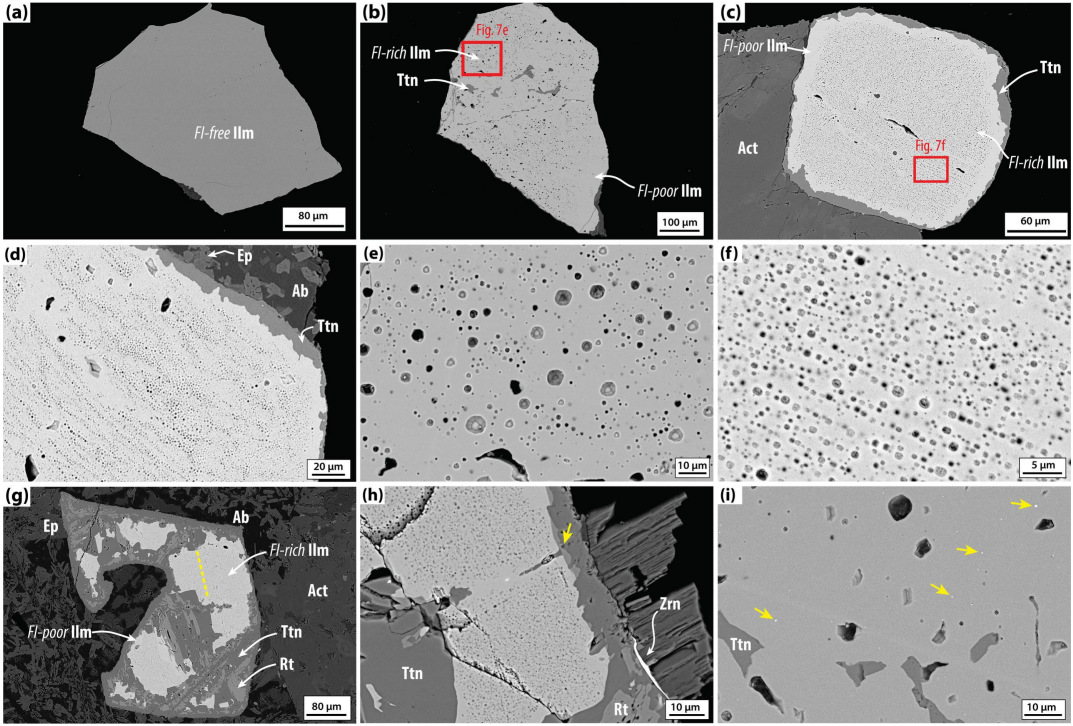
(a)
Fl-free Ilm
80 µm
(b)
Fig. 7e
Fl-rich Ilm
Ttn
Fl-poor Ilm
100 µm
(c)
Fl-poor Ilm
Ttn
Act
Fig. 7f
Fl-rich Ilm
60 µm
(d)
Ep
Ab
Ttn
20 µm
(e)
10 µm
(f)
5 µm
(g)
Ep
Ab
Fl-rich Ilm
Act
Fl-poor Ilm
Ttn
Rt
80 µm
(h)
Zrn
Ttn
Rt
10 µm
(i)
Ttn
10 µm

Figure 7

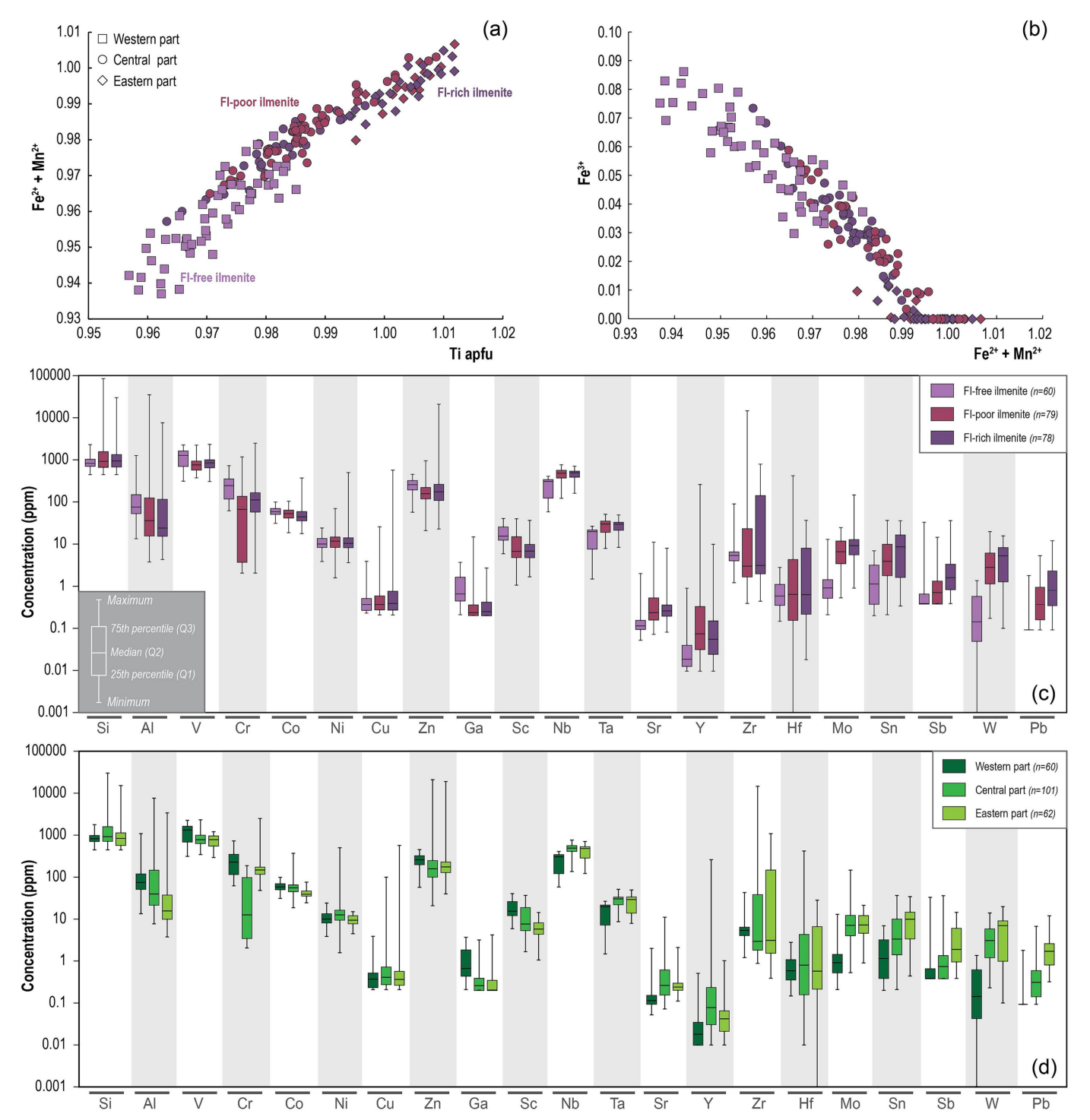
(a)
Western part
Central part
Eastern part
FI-poor ilmenite
FI-rich ilmenite
FI-free ilmenite
Fe2+ + Mn2+
Ti apfu
(b)
Fe3+
Fe2+ + Mn2+
(c)
FI-free ilmenite (n=60)
FI-poor ilmenite (n=79)
FI-rich ilmenite (n=78)
Maximum
75th percentile (Q3)
Median (Q2)
25th percentile (Q1)
Minimum
Concentration (ppm)
Si Al V Cr Co Ni Cu Zn Ga Sc Nb Ta Sr Y Zr Hf Mo Sn Sb W Pb
(d)
Western part (n=60)
Central part (n=101)
Eastern part (n=62)
Concentration (ppm)
Si Al V Cr Co Ni Cu Zn Ga Sc Nb Ta Sr Y Zr Hf Mo Sn Sb W Pb

Figure 8

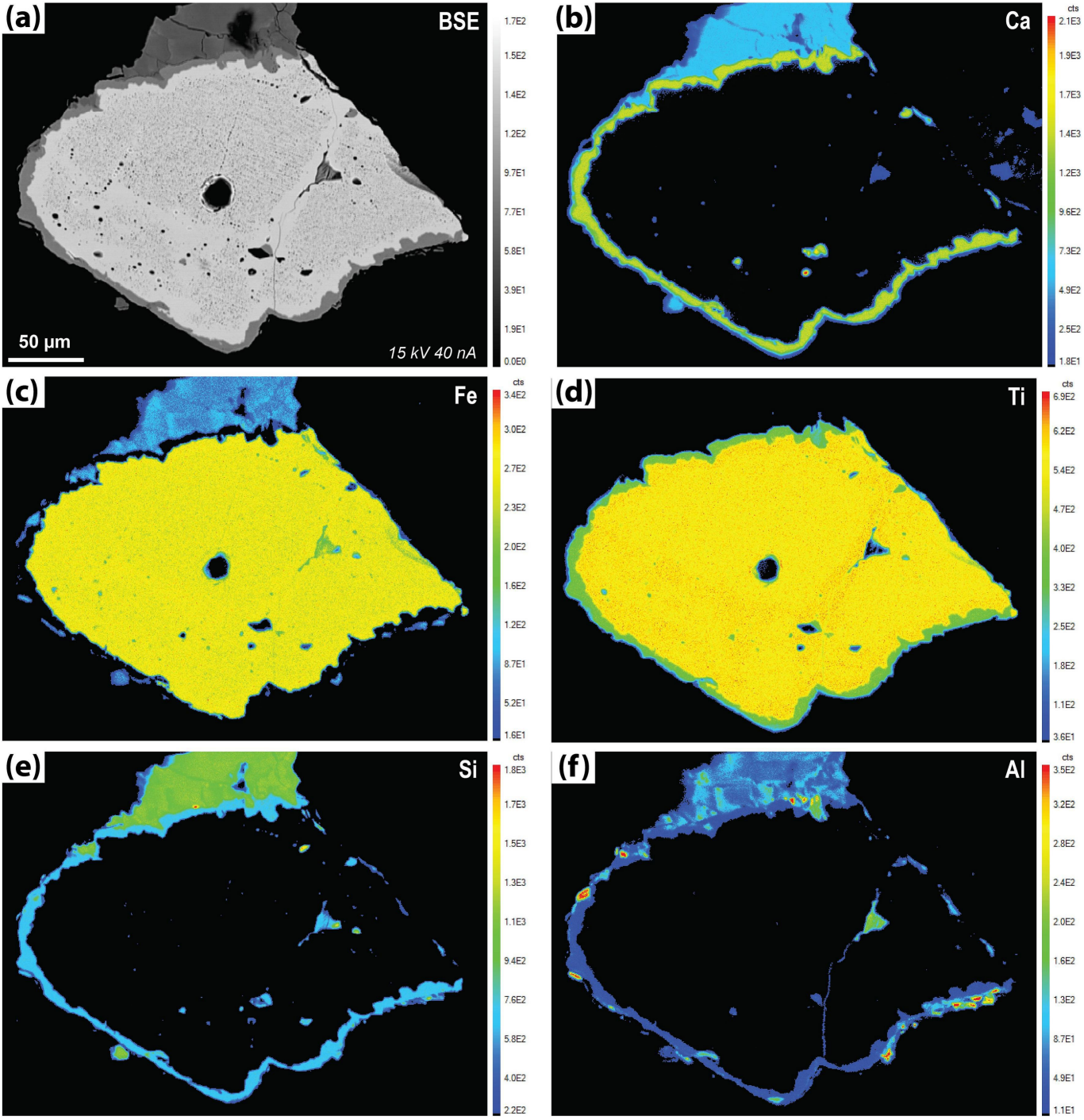
(a)
BSE
50 µm
15 kV 40 nA
1.7E2
1.5E2
1.4E2
1.2E2
9.7E1
7.7E1
5.8E1
3.9E1
1.9E1
0.0E0
(b)
Ca
cts
2.1E3
1.9E3
1.7E3
1.4E3
1.2E3
9.6E2
7.3E2
4.9E2
2.5E2
1.8E1
(c)
Fe
cts
3.4E2
3.0E2
2.7E2
2.3E2
2.0E2
1.6E2
1.2E2
8.7E1
5.2E1
1.6E1
(d)
Ti
cts
6.9E2
6.2E2
5.4E2
4.7E2
4.0E2
3.3E2
2.5E2
1.8E2
1.1E2
3.6E1
(e)
Si
cts
1.8E3
1.7E3
1.5E3
1.3E3
1.1E3
9.4E2
7.6E2
5.8E2
4.0E2
2.2E2
(f)
Al
cts
3.5E2
3.2E2
2.8E2
2.4E2
2.0E2
1.6E2
1.3E2
8.7E1
4.9E1
1.1E1

Figure 9

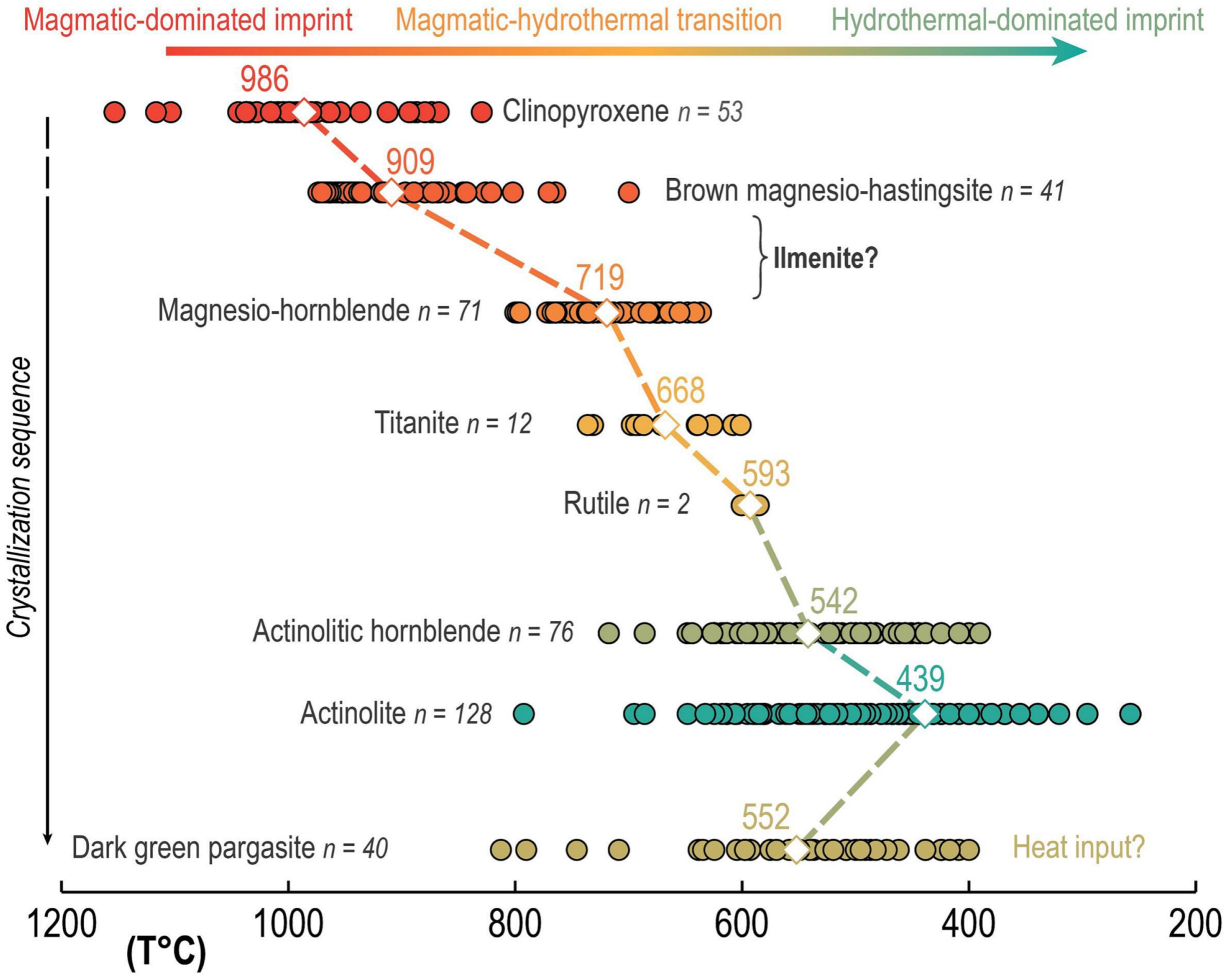
Magmatic-dominated imprint
Magmatic-hydrothermal transition
Hydrothermal-dominated imprint
986
Clinopyroxene n = 53
909
Brown magnesio-hastingsite n = 41
Ilmenite?
719
Magnesio-hornblende n = 71
668
Titanite n = 12
593
Rutile n = 2
542
Actinolitic hornblende n = 76
439
Actinolite n = 128
552
Dark green pargasite n = 40
Heat input?
Crystallization sequence
1200
1000
800
600
400
200
(T°C)

Figure 10

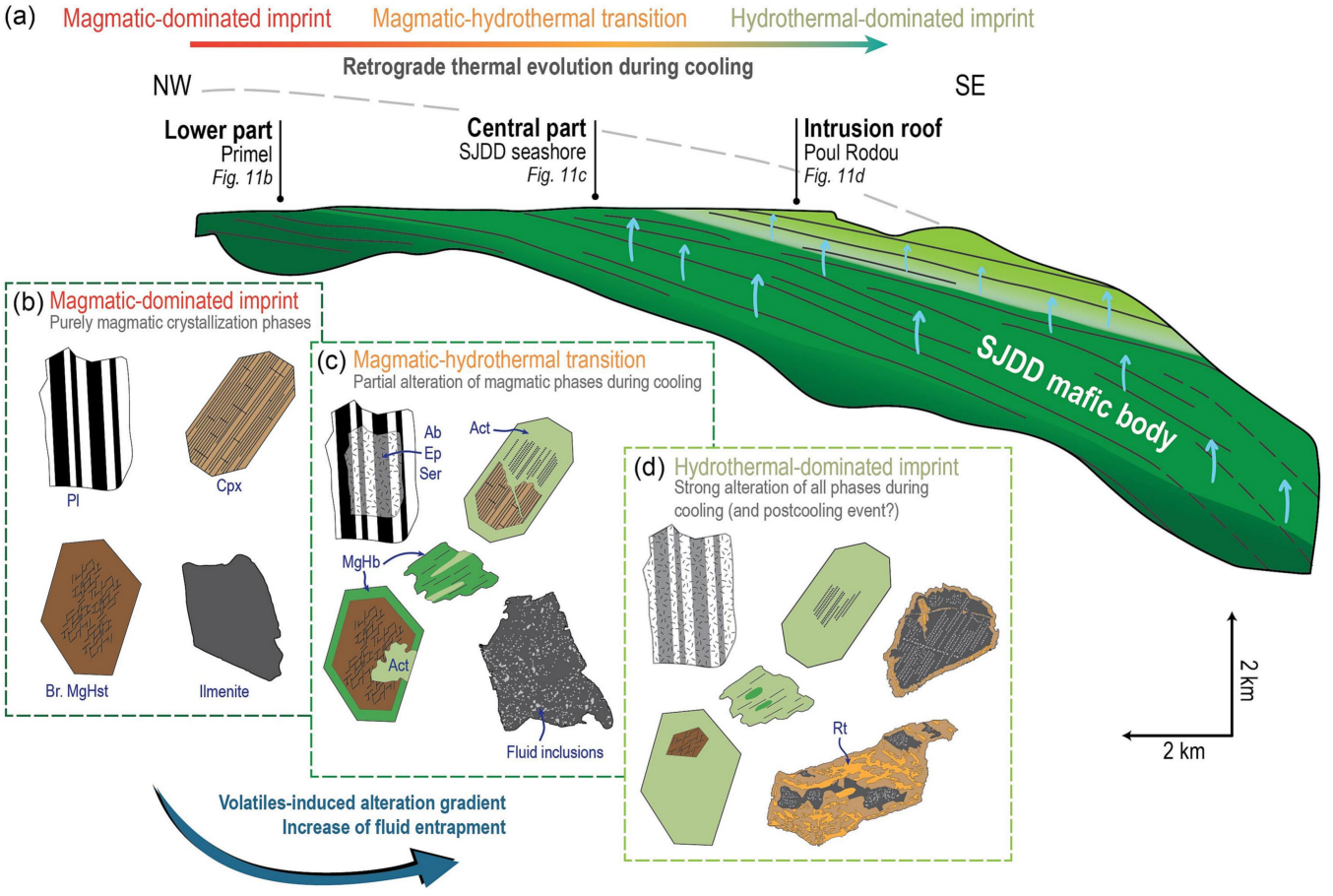
(a)
Magmatic-dominated imprint
Magmatic-hydrothermal transition
Hydrothermal-dominated imprint
Retrograde thermal evolution during cooling
NW
SE
Lower part
Primel
Fig. 11b
Central part
SJDD seashore
Fig. 11c
Intrusion roof
Poul Rodou
Fig. 11d
SJDD mafic body
(b) Magmatic-dominated imprint
Purely magmatic crystallization phases
Pl
Cpx
Br. MgHst
Ilmenite
(c) Magmatic-hydrothermal transition
Partial alteration of magmatic phases during cooling
Ab
Ep
Ser
Act
MgHb
Act
Fluid inclusions
(d) Hydrothermal-dominated imprint
Strong alteration of all phases during cooling (and postcooling event?)
Rt
2 km
2 km
Volatiles-induced alteration gradient
Increase of fluid entrapment

Figure 11